Transpressional zones in ophiolitic mélange terranes: Potential exploration targets for gold in the South Eastern Desert, Egypt

Basem Zoheir

Department of Geology, Faculty of Science, Benha University, 13518 Benha, Egypt

ARTICLE INFO

ABSTRACT

Gold-bearing quartz ± carbonate veins at the El-Anbat mine area, in the South Eastern Desert of Egypt, are associated with pervasively silicified, highly sheared ophiolitic and island arc rocks. Structural analysis of the shear fabrics along the ore zones indicate that geometry of the mineralized quartz veins and alteration patterns are controlled by the regional, NNW-trending zone of transpression, known as the Wadi Kharit–Wadi Hodein shear system, which is related to the 655–540 Ma, Najd strike–slip fault system in the Eastern Desert of Egypt. Microscopic and electron microprobe studies reveal that gold is chemically bound in As-pyrite, arsenopyrite, and gersdorffite, while free-milling gold is rarely observed in the quartz veins and silicified host rocks. Hydrothermal alteration could have liberated additional traces of gold from early pyrrhotite disseminated in listvenite.

Geochemical studies reveal that shear zones associated with lenticular masses of porphyritic granite in the middle of the transpression zone are heavily mineralized (ppm levels) compared with other parts of the alteration zone. Where no granite is observed, low-grade zones (ppb levels) of gold mineralization occur in the highly deformed serpentinite and metavolcaniclastic rocks. Mass balance calculations suggest that hydrothermal fluids infiltrated under brittle–ductile shear conditions led to addition of Au, As, Cu, Rb, and Sb, concurrent with silicification, carbonatization and sericitization of the host rocks. Dispersion of gold and associated pathfinder elements is reported in altered rocks beyond the lode zone, indicating the potential for extensive, low-grade zones outside the already known El-Anbat mine location.

© 2011 Elsevier B.V. All rights reserved.

1. Introduction

Orogenic, vein-type gold deposits typically form during compressional or transpressional tectonics (e.g., Bierlein and Crowe, 2000; Cox et al., 1991; Goldfarb et al., 2005). Gold-base metal mineralization in these deposits commonly forms while the host rocks were being folded and/or reverse-faulted (e.g., Cox et al., 1991; Goldfarb et al., 2005; Sibson et al., 1988). Quartz lodes develop in local extensional sites centered on well-defined fractures in host rocks (Cox et al., 1991; Sibson et al., 1988). Most host rocks are competent and massive on the meter to tens of meters scale during mineralization, so fluid infiltration was chiefly controlled by cleavage foliations and fractures in these competent rocks (Cox et al., 1991; Witt and Vanderhor, 1998).

Within the Pan African Orogen in the Eastern Desert of Egypt, basement domains are bounded by sets of shear zones and normal faults. Both structural elements define a crustal-scale wrench corridor (Unzog and Kurz, 2000). Displacement within this corridor partitioned into orogen-parallel sinistral strike–slip faults and low-angle normal faults, which form extensional bridges between strike–slip faults

(Bregar et al., 1997). Simultaneous activity of both fault systems suggests bulk oblique shortening with consequent orogen-parallel extension (Unzog and Kurz, 2000). Emplacement and/or exposure of the ophiolitic nappes in the Eastern Desert are attributed to transpressive deformation associated with the post-accretionary Najd Fault system (e.g., Abd El-Wahed and Kamh, 2010; Wallbrecher et al., 1993).

Extensive zones of silicification and carbonatization are principally confined to transpressional structures in allochthonous ophiolitic terranes across the Eastern Desert of Egypt. Several studies reported significant gold concentrations in discrete alteration zones in different lithologies (e.g., Botros, 1993; El-Dougdoug, 1990; El-Mezayen et al., 1995; Hassaan et al., 1996; Osman, 1995; Ramadan, 2002; Ramadan et al., 2005). Exposures of intensely sheared ultramafites and carbonatized rocks in the Wadi Hodein area (Ramadan and Kontny, 2004) are confined to discrete shear zones along the major NW–SE Wadi Kharit–Wadi Hodein transpressional corridor (Greiling et al., 1994; Nano et al., 2002). Ramadan (1995) and Ramadan and Kontny (2004) reported gold mineralization in listvenite-type wallrock alteration (~3 km-long and up to 300 m-wide) along the NW and NNW-trending thrust faults, at Gebel El-Anbat area. Temporal and spatial association between gold deposits and zones of transpression in the Eastern Desert is currently receiving attention (e.g., Hassaan et al., 2009; Zoheir, 2008a,b; Zoheir and Lehmann, 2011).

E-mail address: basem.zoheir@gmail.com.

This study reports on the geologic setting, structural control, mineralogy and hydrothermal alteration adjacent to the El-Anbat gold deposit. The lithology and structures that control on gold mineralization and extent of primary geochemical dispersion is based on detailed surface mapping (1:1000) of the mine area. This paper documents the relationship between gold mineralization and regional to local shear zones and discusses features that are relevant to exploration programs targeting orogenic gold-bearing vein and/or disseminated systems in the Eastern Desert of Egypt.

2. Regional geologic/tectonic setting

The Precambrian basement of the Eastern Desert of Egypt is a part of the Arabian–Nubian Shield (ANS), which is dominated by juvenile crust that formed at ~800–600 Ma. Geographic patterns of age, lithology, petrochemistry, and structure have been interpreted in terms of multi-stage development and accretion of intra-oceanic island arcs and inter-vening basins (e.g., Abdelsalam et al., 2003; Kröner et al., 1987; Stern, 1994; Sturchio et al., 1983). The Southern Eastern Desert (SED), one of the three basements provinces defined by Stern and Hedge (1985), contains diverse lithologic assemblage, including granitoid gneisses, ophiolitic and island arc metavolcanic–volcaniclastic–plutonic assemblages (e.g., Stern et al., 1991). The SED is unique among the Egyptian basement provinces in being bounded by the well-defined Allaqi-Heiani and Onib-Sol Hamed sutures (Abdelsalam and Stern, 1996; Abdelsalam et al., 2003; Stern et al., 1991).

Based on published geochronological data, Stern and Hedge (1985) postulate two principal episodes of crustal growth in the SED at 715–700 Ma and 665–685 Ma, comparable to two distinct compressional events described by Sturchio et al. (1983). The first event involved an episode of NW-vergent folding and thrusting, with concomitant magmatic activity. The second event involved compression along a WSW–ENE axis, which initiated uplift, molasse-type sedimentation, large-scale open folding along NNW–SSE axes, and WSW-directed
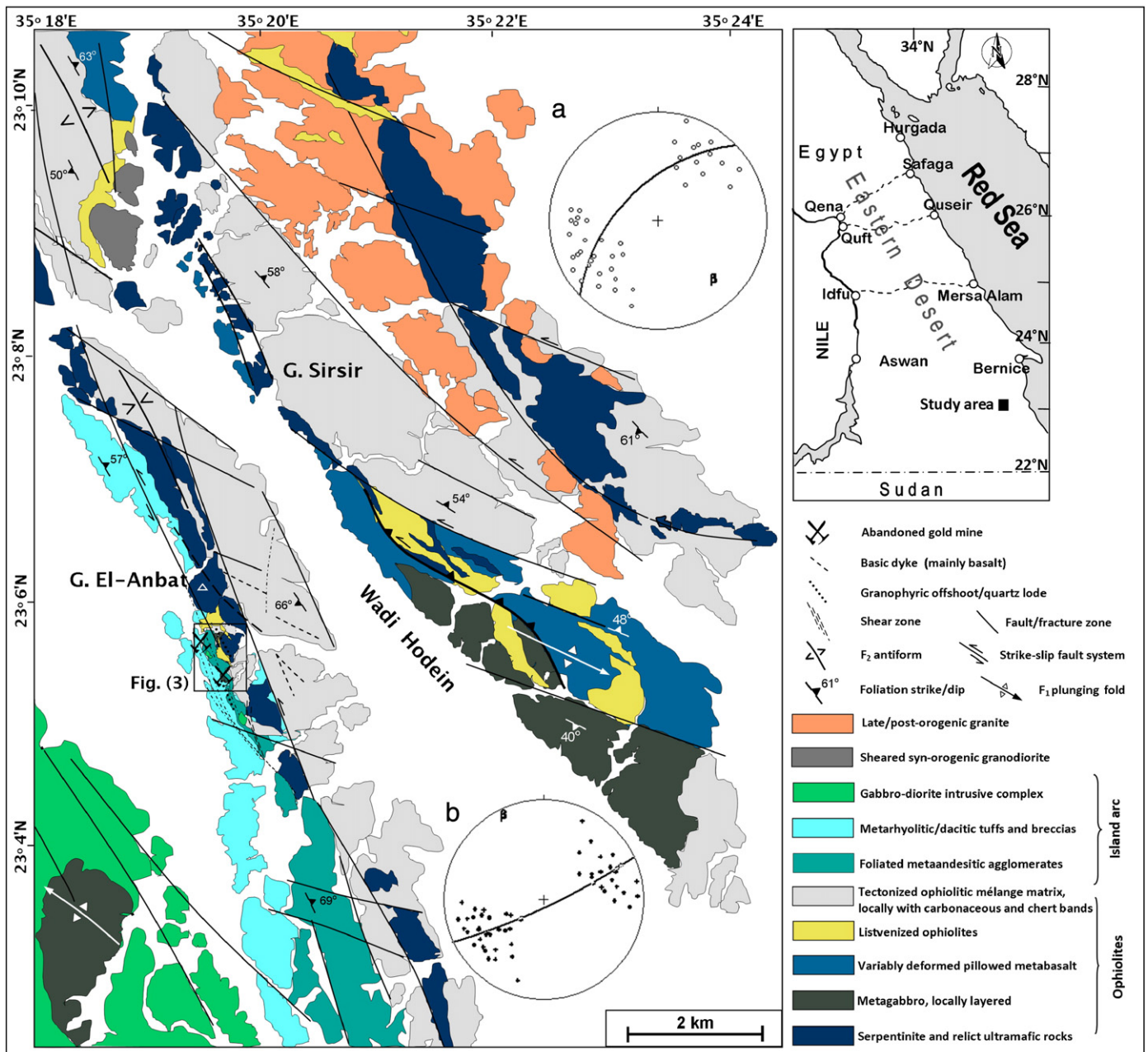

Fig. 1. Geological map of Gebel El-Anbat–Wadi Hodein area. Stereonets refer to foliations and calculated girdles (thick lines) and Beta axes (dashed lines) of F_1 (a) and F_2 (b) folds.

thrusting or gravity sliding. Post-accretionary structures attributed to the second event include major zones of shortening, such as the N-trending Hamisana zone, and the NW-trending Najd strike–slip fault system (Abdeen et al., 2008; Abdelsalam and Stern, 1996; Abdelsalam et al., 2003; Berhe, 1990; de Wall et al., 2001; Stern, 1994). The high angle, sinistral strike–slip Wadi Kharit–Wadi Hodein fault/shear zone is interpreted as an equivalent of the Najd Fault system (e.g., El-Gaby et al., 1988; Stern et al., 1990) and as the youngest major structural element in the Eastern Desert of Egypt (e.g., Fowler and El Kalioubi, 2004; Fritz et al., 1996; Stern, 1985).

3. Geology of the mine area

The Gebel El-Anbat area forms a part of the Neoproterozoic Wadi Hodein district in the SED, where various metamorphic and plutonic rocks are exposed (Fig. 1). Field relationships and high resolution ASTER imagery (i.e., visible near-infrared VNIR bands with 15 m/pixel resolution) enabled detailed mine-scale mapping, which reveal that the study area is underlain by large ophiolitic serpentinite masses tectonically intermixed with the underlying island arc metavolcanic/metavolcaniclastic rocks. Variably sheared blocks of talc carbonate, carbonatized

serpentinite, and foliated metabasalt occur as sheets or lenses along abundant NW and NNW–SSE fault zones, forming the main body of the Sirsir–El-Anbat mountainous series, as well as elongate slices incorporated within volcaniclastic metasediments (Fig. 2a). The latter comprise weakly to strongly foliated polymictic andesitic breccias, agglomerate and less commonly lithic tuffs, generally metamorphosed to greenschist facies assemblage. Most of the ancient gold mining (open pits and shear-parallel trenches) in the area is confined to sheared metavolcaniclastic rocks that exhibit pervasive alteration along a kilometer-scale wide shear zone (Fig. 2b). Variably deformed metagabbro-diorite and granodiorite intrusions cut the metavolcaniclastic rocks.

Porphyritic granite seems to form a series of lenticular apophyses (thin branches or offshoots of granophyre), characterized by disseminated pyrite (up to 5%) and quartz veinlets. These granitic off-shoots cut the metavolcaniclastic rocks and carbonatized serpentinite in the mine area (Fig. 2c and d). The old mine workings extend also to the altered polymictic agglomerate that are exposed in the western part of the mine area, and are characterized by disseminated sulfide associated with abundant chlorite and sericite (fine-grained aggregate of mica-like phases; Rieder et al., 1999) commonly in the fine-grained matrix (Fig. 2e). Blocks of listvenite (potassic metasomatism
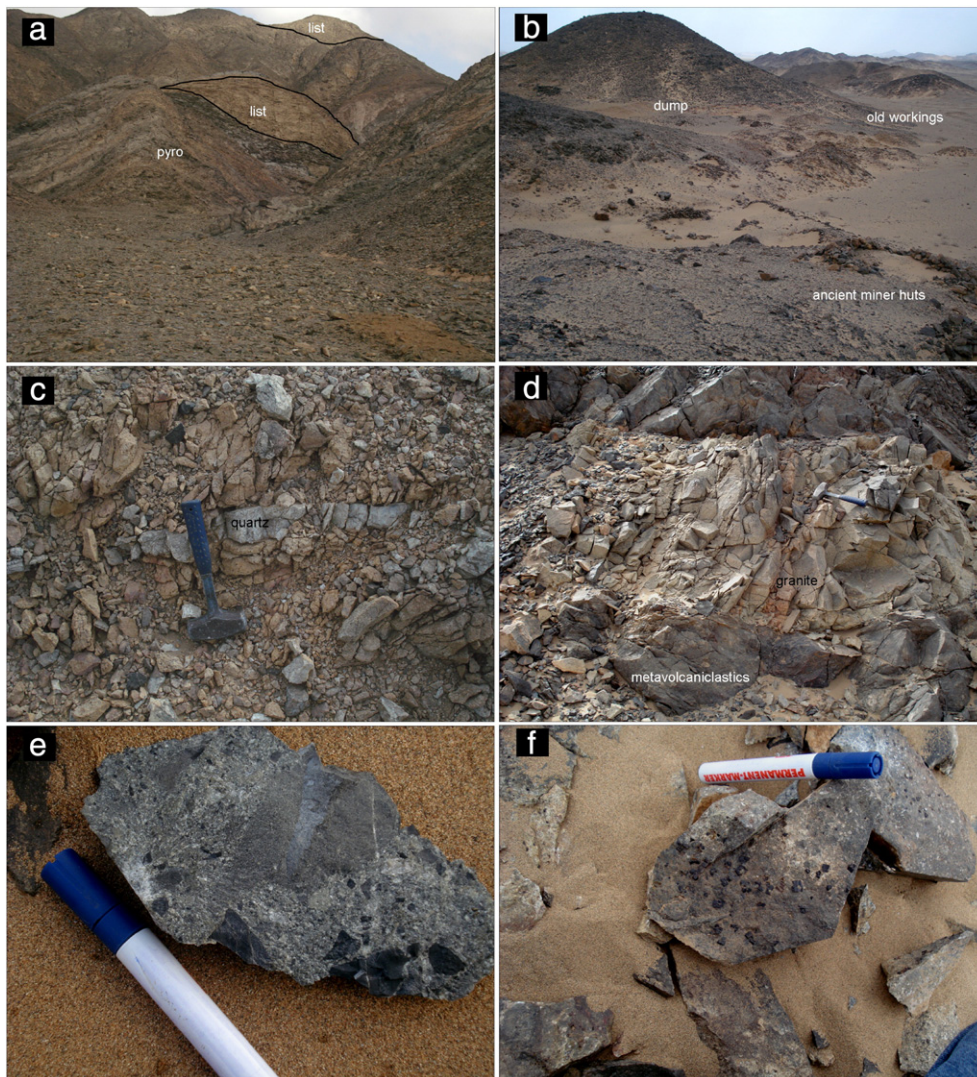
Fig. 2. (a) Highly foliated metavolcaniclastic rocks tectonically interlayered and overlain by the ophiolitic rocks. (Photo looking to East), (b) ancient mining site south of Gebel El-Anbat. Numerous stone huts spread over vast areas in which dumps of quartz veins and altered granitic rocks are abundant (photo looking to the South), (c) quartz lenses intruded into highly altered granitic bodies along worked trench at the mine area. (Photo looking to the North), (d) Granitic dike-like offshoot cutting highly deformed andesitic agglomerates at the El-Anbat mine. (Photo looking to East), (f) hand specimen of polymictic dacitic agglomerates with disseminated sulfides in the sericitized matrix, (e) mineralized listvenite with abundant disseminated, severely oxidized sulfide crystals associated with high content of hydrothermal quartz and sericite.

product of mafic/ultramafic rocks; Halls and Zhao, 1995) are exposed adjacent to thrust structures separating the ophiolites from the underlying metavolcaniclastic rocks. Listvenite is mainly composed of ankerite, quartz, with minor amount of calcite, chlorite, and fuchsite. Magnetite, hematite, and chrome spinels are common opaque minerals in many samples. In the open pits and trenches, listvenite is enriched in disseminated, variably oxidized pyrite crystals (Fig. 2f).

Structurally, the El-Anbat mine area is intensely affected by the regional WSW–ENE compressional regime (the 2nd major tectonic event described above), and related NW-trending folding and WSW-verging thrusting. Widespread criteria of non-coaxial shearing at all scales, i.e., stretching lineations, sets of several kilometer-scale, NW-trending left-stepping folds and superimposed NNW-trending drag folds, and asymmetric crenulations (calculated β axes are 132°/27° and 335°/11°; see Fig. 1) are assumed to have been developed throughout two successive, non-coaxial upright folding increments (F_1 and F_2). Alternatively, the NNW–SSE crenulations and kinks (F_2) could have been developed through oblique non-coaxial deformation of cleaved rocks as Riedel shears (sensu Rajlich, 1993). Conjugate sinistral (N)NW–(S)SE and dextral (E)NE–(W)SW strike–slip faults and shear zones are apparently components of a major transpression system (Fig. 3). At the mine scale, transpression is inferred from mixed shallowly and steeply plunging stretching lineations and abundant sinistral shear indicators. Accordingly, twisting to the NNW–SSE direction and oblique shear on pre-existing NW-SE thrusts may be attributed to the Wadi Kharit–Wadi Hodein shear system, which is related to the 540–655 Ma Najd strike–slip fault system in the Eastern Desert of Egypt (Cole and Hedge, 1986; Greiling et al., 1994; Stacey and Agar, 1985; Stern, 1985).

4. Gold mineralization

Several outcrops of the mineralized, anastomozing (braided) shear zones have been mapped along the main NNW–SSE transpression corridor (Fig. 3). The latter is confined to steeply dipping thrust/fault contacts between variably carbonatized serpentinite and the underlying metavolcaniclastic rocks. A distinct zone of bleached sheared host rocks and disseminated, variably altered pyrite is documented in detail over 1.5 km in a NNW–SSE direction with an average width of 350 m (Fig. 3). This zone is characterized by arrays of quartz pods, granitic offshoots and intermingling carbonate-sericite and malachite

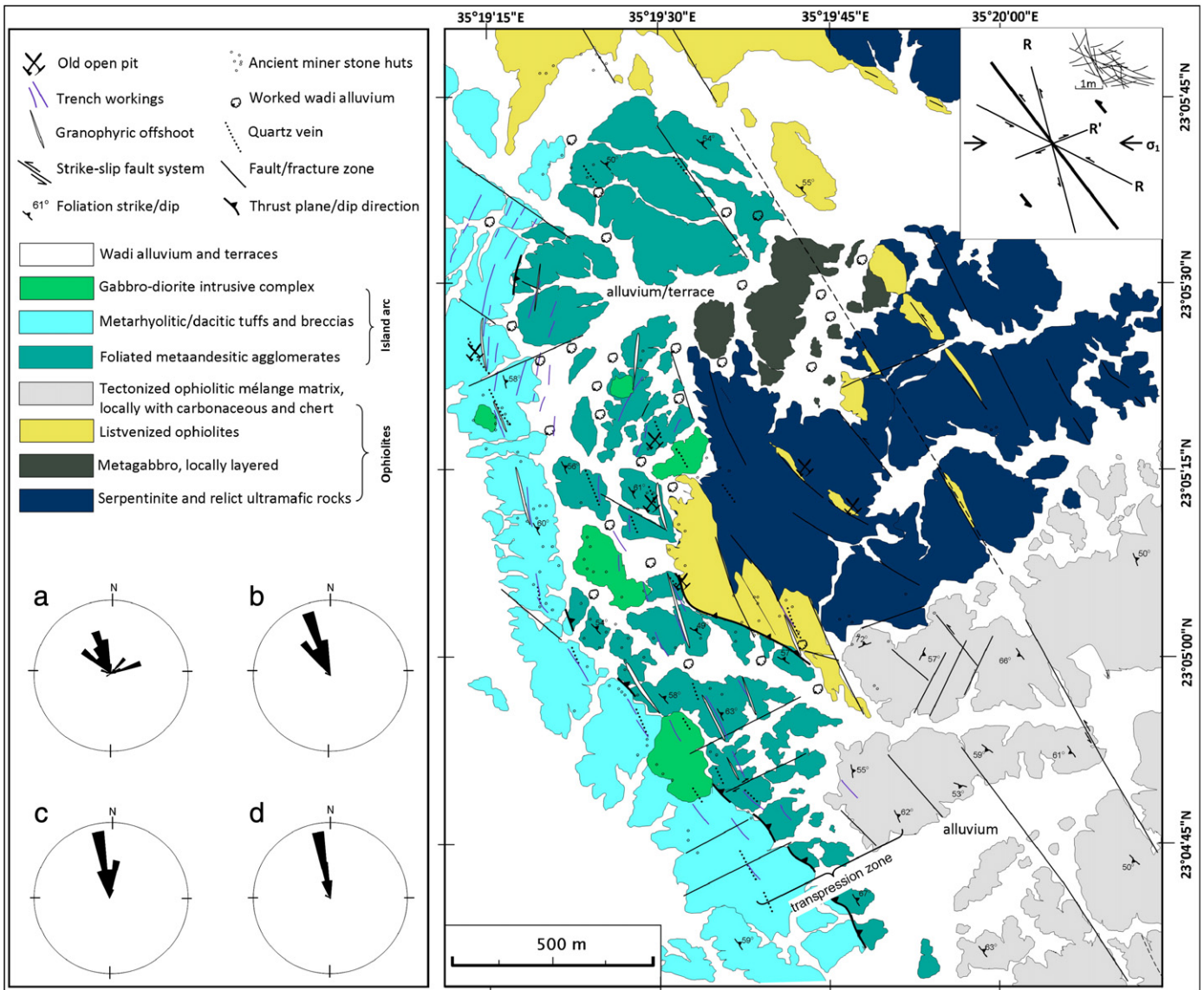**Fig. 3.** Detailed geological map of the El-Anbat mine area illustrating the distribution and attitude of quartz veins, shear planes and granitic offshoots. Inset showing intersecting shear planes in deformed host rocks and geometrical pattern of sinistral shear system (R: Riedel shear, R′ anti-Riedel shear). Rose diagrams refer to (a) strike–slip faults, (b) shear planes, (c) quartz veins, and (d) granitic dike-like offshoots.

veinlets. Variably oxidized pyrite crystals are commonly associated with fracture-filling ankerite and re-crystallized quartz. The mineralized quartz veins may extend for 10 m and their thicknesses vary from a few centimeters to 1 m. In the mine area, silicified listvenite masses and metavolcaniclastic rocks, as well as the sulfidized granitic bodies and carbonate-rich Wadi alluvium has been significantly stopped out, suggesting significant gold grades in the hydrothermally altered, sheared host rocks.

Shear planes are irregularly developed through fissile/cleaved tuffs and agglomerate, with some zones having shears spaced less than 20 cm apart that are separated by massive, less-sheared host rock. Shears in listvenite and metavolcaniclastic rocks are commonly accompanied by fracture arrays at the millimeter to centimeter scales, mostly filled with mixed ankerite and sericite. Quartz lodes and granitic offshoots occur commonly where the foliation is wrapped from NW–SE to NNW–SSE strike directions throughout each of the shear zones. A N-plunging stretching lineation is developed on the vein wall surface and is defined by striation and ridge-groove lineation. S–C fabrics and quartz lenses asymmetry together with widespread NE–SW-striking dilation bends alongside and within the shear zones indicate sinistral sense of shear.

The ore bodies include quartz veins, sulfidized granitic blocks, and pervasively silicified, sulfidized metavolcaniclastics and listvenite (Fig. 4). The main constituents of the quartz veins include quartz, shear/fault gouge, carbonate, and altered wallrock. These constituents are usually mixed dynamically with each other in complex pattern. Vein quartz shows textural patterns varying from comb, ribbon, and brecciated quartz with variable degrees of dynamic re-crystallization (Fig. 5). In addition, microscopic secondary tensional veinlets occur in zones of late joint/fracture intersections. Disseminated S–As minerals are common along shear planes, serrate grain boundaries or disseminated in slivers of chlorite-rich wallrock. In many cases, aggregated grains are observed where shear planes are distorted (Fig. 5). This observation suggests that the S-As mineral assemblage formed synchronous with shearing. An association between sulfide minerals

and sericite $\pm$ chlorite assemblage is distinct in all host rock varieties. Intense brecciation and (or) boudinage of the granitic bodies and host rocks is observed where shears cut through different lithologies.

5. Ore mineralogy

Ore microscopy aided by SEM (scanning electron microscope) investigations of the quartz lodes and adjacent altered wallrocks revealed the presence of disseminated pyrite, pyrrhotite, chalcopyrite, subordinate pentlandite, arsenopyrite, and gersdorffite, and scarce microscopic gold. Most listvenite samples and a few samples of andesitic breccia/agglomerate and quartz lode contain magnetite $\pm$ hematite and relicts or selvages of chrome spinel crystals commonly associated with mixtures of carbonate and chlorite (Fig. 6a). The quartz lodes contain idiomorphic to xenomorphic pyrite crystals with abundant inclusions of chalcopyrite (Fig. 6b). In most samples, pyrite is variably altered into goethite. Arsenopyrite occurs as dispersed subhedral crystals confined to micro-fissures in quartz veins and is locally replaced by iron-hydroxides (Fig. 6c). A few micron-large arsenopyrite inclusions have been observed in some pyrite grains disseminated in the granitic rocks and quartz veins (Fig. 6d). Fine-grained, dispersed anhedral pentlandite grains are associated with pyrite in quartz lodes and altered wallrocks (Fig. 6e). Chalcopyrite and pyrrhotite are subordinate, occurring chiefly as dispersed globules intergrown with pentlandite and pyrite (Fig. 6f). Free-milling gold occurs as patchy globules in the quartz veins (Fig. 6g) or as blebs dispersed in sericite-carbonate masses in the wallrocks (Fig. 6h).

Table 1 reports the electron microprobe analyses of ore minerals disseminated in altered wallrocks and quartz veins at the El-Anbat mine area. Analytical data were obtained on a CAMECA Camebax SX-100 electron microprobe at the Institute of Mineralogy and Mineral Resources, Technical University of Clausthal (Germany). The accelerating voltage applied was 30 kV, and beam current varied from 40 to 100 nA. The beam was defocused at 1–5 μm, and the counting time between 10 and 120 s. The high voltage and beam current
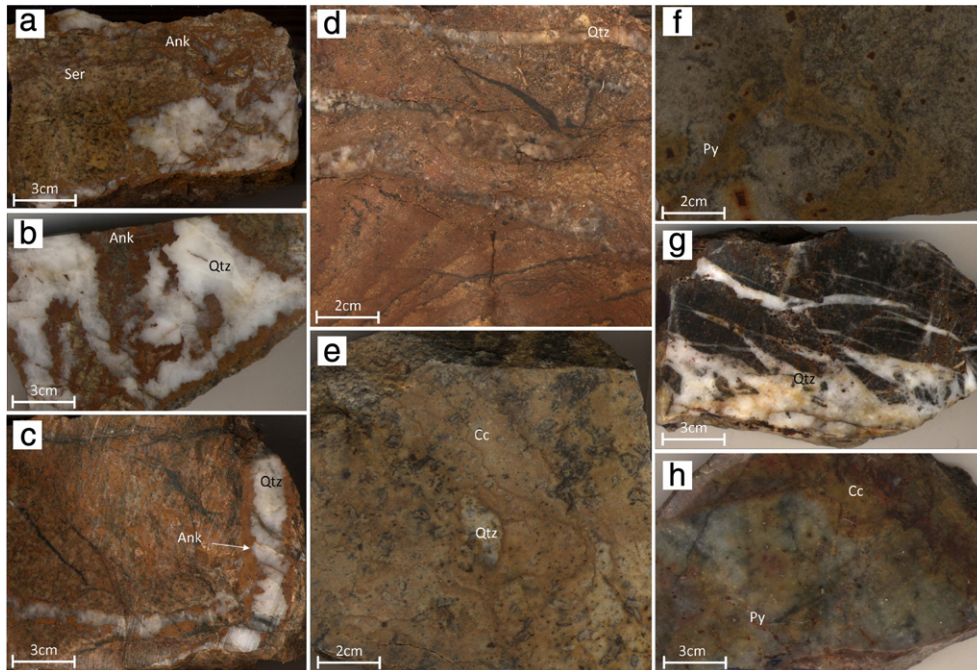
Fig. 4. Characteristics of the different ore bodies at the El-Anbat mine. (a) and (b) Milky quartz pods and associated ankerite and sericite in mineralized listvenite, (c) quartz veins and associated ankerite defining a NNW–SSE drag fold later affected by coaxial fracture system filled with mixture of carbonate and carbonaceous material, (d) quartz veinlets cut foliation planes in silicified listvenite. Foliation is defined by alternating quartz-rich and carbonate-rich bands, (e) quartz and calcite (Cc) pockets along parallel shears in a mineralized granitic offshoot, (f) intensely carbonatized dacitic agglomerate with abundant disseminated altered pyrite and associated sericite seams, (g) fracture-filling quartz stringers along slip planes in tectonized gabbroic rock, (h) pyrite-rich quartz vein with disseminated pyrite crystals and carbonate (i.e., calcite).
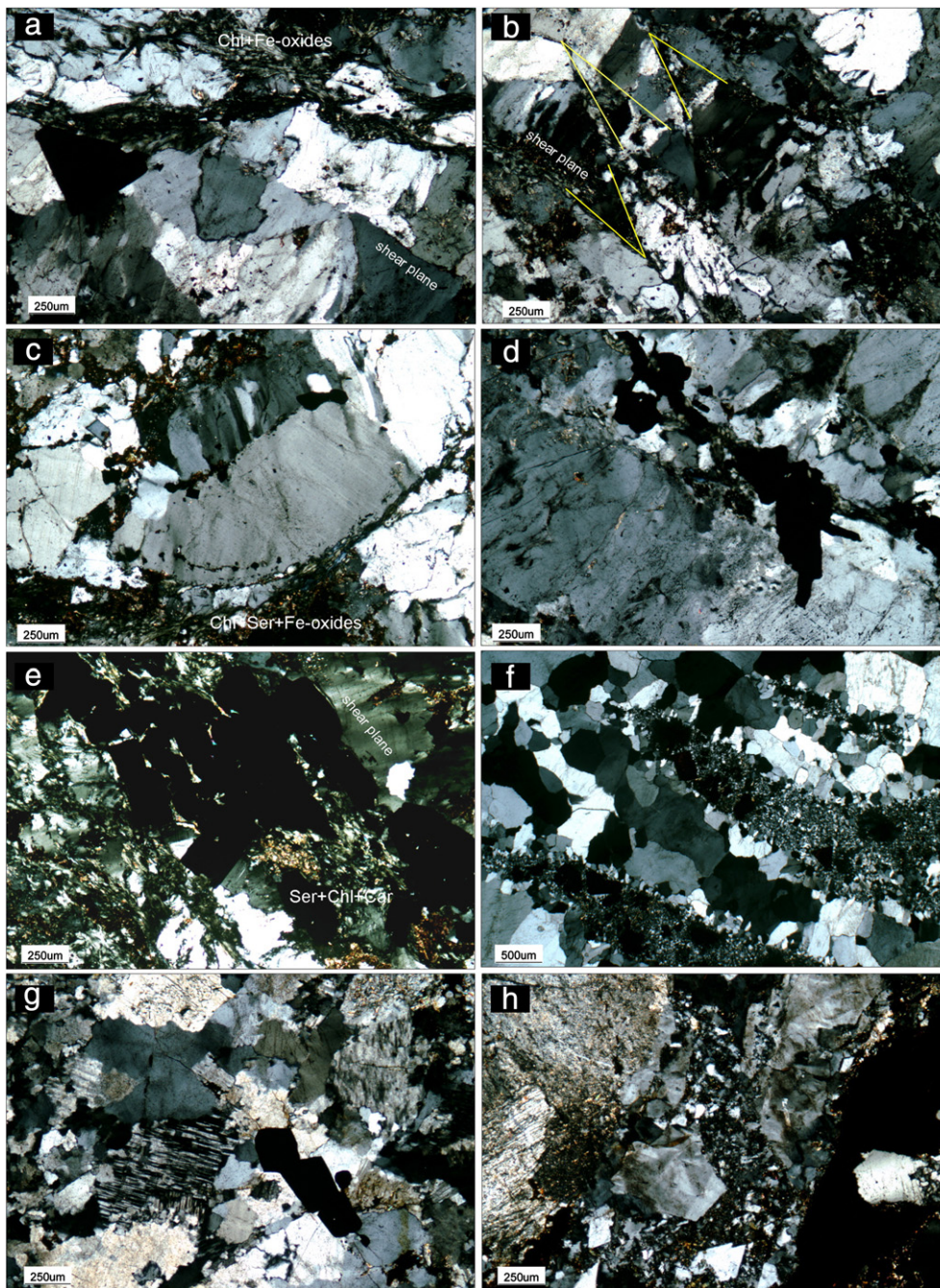
Fig. 5. Features of the mineralized quartz veins and granitic offshoots. (Crossed polars photomicrographs): (a) Blocky microstructure in mineralized quartz vein, where large quartz crystals are separated either by discrete slip surfaces or by slivers of foliated wallrocks mainly of chlorite (Chl) and Fe-oxides composition, (b) pervasive conjugate shear bands in mineralized quartz veins exhibiting sub-grain development along the shear planes (yellow lines), (c) and (d) disseminated sulfide crystals along grain boundaries of ribboned quartz prophyroblast showing deformation lamellae. Notice the abundant selvages of sericite (Ser), chlorite and carbonate (Car), (e) preferably oriented sulfide aggregated crystals associated with sericite, chlorite and fine-grained hydrothermal quartz, (f) mineralized quartz vein showing alternation of tabular zones with internal elongated blocky microstructures and deformed domains with dynamically recrystallized quartz crystals and slivers of chlorite-rich wallrock, (g) sulfide-bearing granitic offshoot with interstitial hydrothermal quartz, (h) brecciated granitic offshoot with interstitial hydrothermal quartz and abundant disseminated sulfide minerals and carbonate.

accelerating conditions applied as well as the long counting time were aimed at improving the detection limit of the electron microprobe used (e.g., Fialin et al., 1999; Jercinovic and Williams, 2005; Robinson et al., 1998 and references therein).

The electron microprobe studies reveal the presence of two varieties of pyrite (Table 1), namely As-bearing (type I) and As-barren (type II). Type I pyrite occurs as 100 s μm-long idiomorphic crystals associated with fine-grained arsenopyrite and gold specks. It contains 0.32–1.85 wt.% As, and more rarely traces of refractory gold

(up to 0.11 wt.%). Nickel is almost absent in this pyrite variety. Type II variety is fine-grained, subhedral to idiomorphic pyrite commonly associated with pentlandite and pyrrhotite in slivers of listvenite in quartz lodes. It shows traces of Ni (0.05–0.12 wt.%) and Cu (up to 0.18 wt.%). The composition of arsenopyrite from the El-Anbat deposit includes refractory Au (ave. 0.25 wt.%), Ni (0.13–0.28 wt.%), and Co (up to 0.19 wt.%). The backscattered electron image and microprobe analyses reveal that arsenopyrite crystals are un-zoned, with invariable As and Au contents in cores and rims. Calculated at.% As
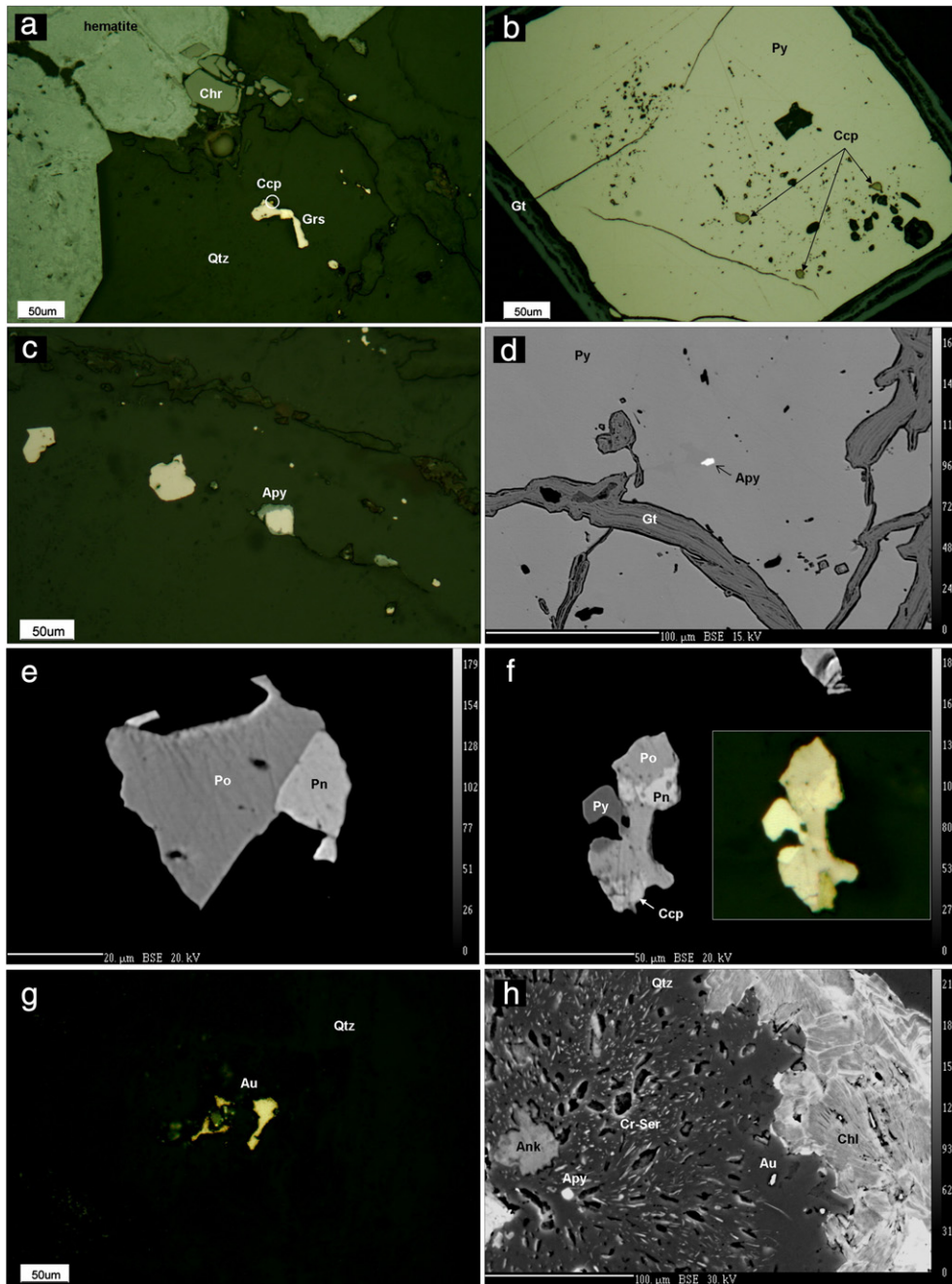
Fig. 6. Photomicrographs of the ore minerals of El-Anbat gold deposit. (a) Relict chromite (Chr) replaced by iron oxides/hydroxides and disseminated gersdorffite (Grs) and chalcopyrite (Ccp) in quartz vein sample. (Polished section, plane polarized light, ×200, air), (b) chalcopyrite (Ccp) inclusions in large euhedral, As-barren pyrite (Py) disseminated in quartz lodes cutting listvenite. (Plane polarized light), (c) Subhedral arsenopyrite (Apy) crystals confined to micro-fissures in quartz veins. (Plane polarized light), (d) Arsenopyrite (Apy) inclusions in As-bearing pyrite disseminated in granophyric offshoot. Notice that goethite replaces pyrite along inherited microfractures and growth boundaries. (BSE), (e) intergrown pyrrhotite (Po) and pentlandite (Pn) dispersed in vein quartz. (BSE), (f) Composite grain of intergrown pyrite–pyrrhotite–pentlandite–chaclopyrite (BSE). Inset showing the reflected light view of the same grain, (g) globules of gold (Au) filling fractures and voids in quartz lodes. (Plane polarized light, oil immersion), (h) Chlorite (Chl) flakes and sericite (Ser) fibers in association with ankerite (Ank) in a silica-rich listvenite sample. Notice the presence of micron-sized arsenopyrite (Apy) and gold specks. (BSE).

of the analyzed arsenopyrite grains (30.2–31.6) suggest formation temperatures varying between 315 and 400 °C (cf. Kretschmar and Scott, 1976). Gersdorffite is commonly associated with arsenopyrite and processes average composition formulated as $Fe_{0.33}Ni_{0.75}As_{0.94}S_{0.96}$. Pyrrhotite is Ni-bearing, with compositions vary from $Fe_{0.92}Ni_{0.02}S_{1.06}$ to $Fe_{0.8}Ni_{0.2}S_1$. Several hundreds of ppms of Au are indicated by the electron microprobe data of pyrrhotite (Table 1). Ni-rich minerals commonly associated with pyrrhotite form specks dispersed in quartz veins and slivers of wallrocks. These minerals vary in composition from horomanite ($Fe_6Ni_3S_8$) to pentlandite and/or godlevskite ($Fe_{4.3}Ni_{4.7}S_8$). Chemically, the electron microprobe data

suggest a complete solid solution series from Ni-bearing pyrrhotite through nickeliferous pyrrhotite to pentlandite, in which Ni varies from 0.6 to 38.6, Fe from 29.5 to 59.1, and S between 31.2 and 38.9 wt.% (Table 1). Fe/(Ni + Fe) approaches 1 in pyrrhotite, and decreases systematically through the solid solution phases until reaching 0.43–0.48 in pentlandite (Table 1). End members in the calculated formula of pentlandite are FeAsS (0.25–0.27), NiAsS (0.71–0.74) and CoAsS (0.01–0.02). Chalcopyrite has a nearly stoichiometric composition ($Cu_1Fe_{1.06}S_{1.93}$), and contains low concentrations of Ni (≤0.38 wt.%) and Zn (up to 0.23 wt.%). Gold grain compositions are mainly high fineness electrum with traces of Te and Sb (Table 1).

Table 1

Representative EPMA data of sulfide minerals disseminated in mineralized quartz lodes and altered wallrocks from the El-Anbat gold mine.

Wt.%	Ni-pyrrhotite							Nickeliferous pyrrhotite–horomanite solid solution						Pentlandite–Godlevskite				
Fe	58.24	57.75	58.65	58.60	59.06	58.93	58.48	51.74	49.08	50.03	43.30	43.30	44.20	29.50	30.56	31.55	29.68	30.70
S	38.70	38.36	38.25	38.75	38.46	38.86	38.19	36.50	34.15	36.26	32.37	33.14	33.22	32.52	32.16	33.16	31.16	32.31
As	–	0.05	–	–	–	–	–	–	0.04	0.02	–	–	0.02	–	0.04	–	–	–
Co	–	–	–	–	–	–	–	–	–	–	–	–	–	–	–	–	–	–
Ni	1.30	1.91	1.93	0.57	1.37	1.15	1.43	11.29	15.68	13.09	23.11	22.79	21.53	36.57	36.70	34.00	38.62	35.75
Cu	–	–	–	–	–	–	–	–	–	–	–	0.03	0.01	–	–	–	0.02	–
Zn	0.00	0.01	0.01	0.02	0.02	0.01	0.03	0.02	–	–	–	–	0.02	0.03	–	–	0.02	–
Ag	0.03	0.02	0.04	0.05	–	0.03	0.05	–	–	0.04	0.04	0.02	0.03	0.02	0.03	–	–	0.02
Te	–	–	–	–	–	0.02	–	–	–	–	–	–	–	–	–	–	–	–
Au	0.07	0.04	0.09	0.12	0.07	0.08	0.11	–	–	–	–	–	–	–	–	–	–	–
Sb	–	–	–	–	–	–	–	–	–	–	–	–	–	–	–	–	–	–
Sum	99.32	99.11	99.94	99.10	99.98	100.1	99.27	100.4	99.77	100.3	99.50	99.96	99.70	99.10	99.94	99.25	99.93	99.25
Fe/(Ni + Fe)	0.98	0.97	0.97	0.99	0.98	0.98	0.98	0.82	0.76	0.79	0.65	0.66	0.67	0.45	0.45	0.48	0.43	0.46

Wt.%	As-bearing pyrite							As-barren pyrite							Gold		
Fe	47.09	47.15	47.30	47.08	47.23	47.03	47.01	47.33	47.20	46.75	46.85	47.23	47.26	47.22	0.43	0.12	0.25
S	52.18	51.89	52.18	51.78	51.78	51.93	51.64	51.93	51.79	50.76	50.41	51.61	51.44	51.91	–	–	–
As	–	0.04	–	–	–	0.03	–	0.02	–	1.85	1.80	0.63	0.64	0.32	–	–	–
Co	–	–	–	–	–	–	–	–	–	–	–	–	–	–	–	–	–
Ni	0.09	0.10	0.06	0.08	0.07	0.12	0.05	0.06	0.12	–	–	–	–	–	–	–	–
Cu	0.07	0.09	–	0.18	0.11	0.13	0.06	–	–	–	–	–	–	–	–	–	–
Zn	–	–	–	0.02	0.03	–	0.02	–	–	–	0.03	–	–	–	–	–	–
Ag	0.04	0.03	–	0.05	0.02	0.04	0.03	0.03	0.03	0.04	0.03	–	–	0.03	9.41	11.36	10.50
Te	–	–	0.02	–	–	–	–	0.04	–	0.02	–	–	–	–	0.21	0.18	0.15
Au	–	–	–	–	–	–	–	–	–	0.11	0.09	–	0.08	0.03	89.26	87.26	88.06
Sb	–	–	–	–	–	–	–	–	–	–	–	–	–	–	–	0.06	0.03
Sum	99.48	99.32	99.61	99.19	99.24	99.29	98.81	99.42	99.16	99.53	99.21	99.51	99.44	99.52	99.31	98.98	98.99

Wt.%	Chalcopyrite							Gersdorffite			Arsenopyrite							
Fe	30.88	31.87	31.88	32.01	30.74	31.43	31.78	10.63	11.18	10.33	34.69	34.56	34.95	34.77	34.16	33.01	35.43	34.28
S	33.68	32.47	33.16	32.70	33.27	33.41	33.20	18.78	18.27	18.33	21.08	20.89	19.93	21.81	20.26	21.87	20.35	20.86
As	–	–	–	–	–	–	–	43.19	42.24	43.67	42.22	43.55	43.04	42.58	43.19	43.02	42.63	42.77
Co	–	–	–	–	–	–	–	0.54	0.54	0.59	0.06	0.10	0.19	0.05	0.12	0.07	0.15	0.06
Ni	0.28	0.08	0.06	0.22	0.15	0.38	0.12	26.77	26.67	25.79	0.16	0.14	0.13	0.28	0.14	0.20	0.13	0.23
Cu	33.52	33.75	33.98	34.16	34.09	34.28	34.18	–	–	–	–	–	–	–	–	–	–	–
Zn	0.02	–	0.03	0.09	0.11	0.23	–	0.03	–	–	–	–	–	0.03	–	0.02	–	0.03
Ag	–	–	–	–	–	–	–	–	–	–	–	–	–	–	–	–	–	–
Te	–	–	–	–	–	–	–	–	–	–	–	–	–	–	–	–	–	–
Au	–	–	–	–	–	–	–	0.13	0.12	0.14	0.24	0.21	0.24	0.26	0.23	0.22	0.22	0.23
Sb	–	–	–	–	–	–	–	0.04	0.04	0.02	–	0.06	–	0.04	–	0.05	–	0.04
Sum	98.40	98.18	99.14	99.19	98.36	99.73	99.30	100.1	99.08	98.88	98.45	99.54	98.51	99.83	98.11	98.48	98.94	98.51
FeAsS								0.29	0.30	0.29	0.99	0.99	0.99	0.99	0.99	0.99	0.99	0.99
NiAsS								0.70	0.68	0.69								
CoAsS								0.01	0.01	0.02								

– below detection limit.

5.1. Chrome spinel

Composition of disseminated chrome spinel crystals has been determined using the electron microprobe technique, applying accelerating voltage of 15 kV, and beam current of 20 nA. Although generally MnO- and TiO_2-poor (<0.1 wt.%), the investigated chrome spinel grains show a compositional zoning with a Cr-rich core to Fe-rich rim (Table 2). Large crystals disseminated in the wallrocks and occasionally as selvages in the quartz veins are characterized by variable, but generally high chromite components Cr# [Cr/(Cr + Al)] (0.53–0.81), and variable Mg# [Mg/(Mg + Fe^{II})] values (0.31–0.58). The compositional zoning in the analyzed spinels is usually the result of enrichment in Cr relative to Al in the rims, accompanied by an increase in the Fe^{II}/(Fe^{II} + Mg) ratio (Table 2). However, in some spinel grains the compositional zoning is almost entirely due to an increase in Fe^{II}/(Fe^{II} + Mg) value towards the spinel rim (Table 2). The analyzed spinel gains pertain to Al-chromite and fall within the ophiolitic chromitite field and/or overlap with the boninitic field (Fig. 7). The high Cr#, low TiO_2 contents, coupled with Al_2O_3 contents range between 9 and 22 wt.% may suggest a supra-subduction zone tectonic setting and a back-arc origin for the ophiolitic rocks (sensu Barnes and Roeder, 2001; Kamenetsky et al., 2001). Calculated assuming chromite stoichiometry, the highly variable ferrous/ferric iron ratios (6–

34) may indicate partial oxidation of ferrous to ferric iron during low grade metamorphism and/or hydrothermal alteration.

6. Hydrothermal alteration

Hydrothermal alteration zones marginal to vein-type gold deposits is important for understanding the genesis of gold mineralization and can be used as a guide for exploration (e.g., Li et al., 1998). Despite a complex distribution of alteration phases, geological mapping, combined with petrography and whole-rock geochemistry indicate that most rock units in the mine area have been replaced by hydrothermal assemblages that define a gross hydrothermal halo surrounding the ore zones. Alteration shows up as sericite–ankerite-rich zones with disseminated altered pyrite and variably developed quartz veins, breccias and silicification zones (see Fig. 3). The common alteration mineral phases associated with disseminated sulfides in altered wallrocks and quartz lodes include sericite, chlorite, and carbonate. The following is discussion of the petrographic features and chemical composition of these phases, based on microscopic and electron probe data. In addition, characterization of the element enrichments and depletions in the host rocks due to infiltration of the hydrothermal fluids is presented in a following section.

Table 2
Representative EPMA data of chrome spinel grains disseminated in mineralized quartz lodes and altered wallrocks from the El-Anbat gold mine.

	Core	Rim	Core	Rim	Core	Rim	Core	Rim	Core	Rim	Core	Rim	Core	Rim
SiO_2	–	0.01	0.02	0.01	0.02	0.01	0.03	0.00	0.03	0.02	0.02	0.01	0.03	0.05
TiO_2	0.06	0.05	0.08	0.06	0.01	0.07	0.04	0.03	0.04	0.08	0.05	0.07	0.06	0.04
Al_2O_3	21.17	20.71	21.90	20.57	21.68	18.49	21.90	16.51	17.33	9.53	9.45	8.96	20.74	17.67
Cr_2O_3	48.25	45.60	45.79	46.70	48.53	49.71	46.88	49.57	51.85	60.18	59.97	56.94	47.56	50.32
V_2O_3	0.32	0.29	0.37	0.29	0.29	0.21	0.25	0.36	0.37	0.33	0.29	0.26	0.30	0.23
FeO	17.71	24.90	23.68	23.87	17.11	21.57	20.77	25.15	17.68	17.78	18.37	27.27	22.36	23.25
MnO	–	–	–	–	–	–	–	–	–	–	–	–	–	–
MgO	12.38	7.04	8.37	7.71	12.63	8.91	10.18	6.21	11.90	11.06	10.84	6.41	10.20	8.61
CaO	–	0.01	0.01	–	–	0.01	–	–	–	0.02	–	–	0.01	–
ZnO	0.16	0.82	0.68	0.53	0.16	0.28	0.29	0.59	0.15	0.13	0.11	0.67	0.24	0.22
NiO	0.02	0.08	0.02	0.08	0.09	0.04	0.06	0.07	0.04	0.05	0.06	0.04	0.06	0.01
Total	100.07	99.51	100.92	99.82	100.52	99.30	100.40	98.49	99.39	99.18	99.16	100.63	101.56	100.40
Formula units based on 4 oxygens and Fe^{II}/Fe^{III} assuming full site occupancy and chromite stoichiometry														
Si	0.00	0.00	0.00	0.00	0.00	0.00	0.00	0.00	0.00	0.00	0.00	0.00	0.00	0.00
Ti	0.00	0.00	0.00	0.00	0.00	0.00	0.00	0.00	0.00	0.00	0.00	0.00	0.00	0.00
Al	0.77	0.79	0.81	0.78	0.79	0.70	0.81	0.65	0.65	0.37	0.37	0.36	0.76	0.67
Cr	1.18	1.17	1.14	1.19	1.18	1.27	1.16	1.31	1.30	1.57	1.57	1.52	1.17	1.28
V	0.01	0.01	0.01	0.01	0.01	0.01	0.01	0.01	0.01	0.01	0.01	0.01	0.01	0.01
Fe^{III}	0.03	0.03	0.03	0.02	0.02	0.02	0.02	0.03	0.04	0.04	0.05	0.11	0.06	0.04
Fe^{II}	0.43	0.64	0.59	0.62	0.42	0.57	0.52	0.68	0.43	0.45	0.46	0.66	0.52	0.58
Mn	0.00	0.00	0.00	0.00	0.00	0.00	0.00	0.00	0.00	0.00	0.00	0.00	0.00	0.00
Mg	0.57	0.34	0.39	0.37	0.58	0.43	0.47	0.31	0.56	0.55	0.54	0.32	0.47	0.41
Ca	0.00	0.00	0.00	0.00	0.00	0.00	0.00	0.00	0.00	0.00	0.00	0.00	0.00	0.00
Zn	0.00	0.02	0.02	0.01	0.00	0.01	0.01	0.01	0.00	0.00	0.00	0.02	0.01	0.01
Ni	0.00	0.00	0.00	0.00	0.00	0.00	0.00	0.00	0.00	0.00	0.00	0.00	0.00	0.00
Total	3.00	3.00	3.00	3.00	3.00	3.00	3.00	3.00	3.00	3.00	3.00	3.00	3.00	3.00
$Fe^{II}/Fe^{II}+Mg$	0.43	0.65	0.60	0.63	0.42	0.57	0.52	0.69	0.44	0.45	0.46	0.67	0.53	0.59
$Cr/Cr+Al$	0.60	0.60	0.58	0.60	0.60	0.64	0.59	0.67	0.67	0.81	0.81	0.81	0.61	0.66
$Mg/(Mg+Fe^{II})$	0.57	0.35	0.40	0.37	0.58	0.43	0.48	0.31	0.56	0.55	0.54	0.33	0.47	0.41
Fe^{II}/Fe^{III}	12.73	19.93	19.09	27.85	18.08	33.57	22.64	25.04	12.36	11.55	9.99	6.07	9.02	14.48

– below detection limit.

6.1. Sericite

Sericite is a ubiquitous component in all altered host rocks in the mine area. Sericite disseminated in sulfide-bearing listvenite is generally fine-grained (ca. 20 μm) and is commonly intimately intergrown with quartz-carbonate ± chlorite assemblages. It is mainly Cr-bearing sericite (fuchsite), containing from traces up to 2.27 wt.% Cr_2O_3 (Table 3). The source of chromium is likely the hydrolysis of olivine or chrome spinels (cf. Savage et al., 2000) in the parental ultramafic rocks. Calculated on basis of 22 anions, the structural formulae of fuchsite comprise tetrahedral Si of 6.06–6.37, 1.463–1.94 Al^{IV}, 3.19–3.57 Al^{VI}, 1.29–1.85 K, 0.15–0.28 Mg, 0.45–0.68 Fe, 0.03–0.07 Na, and Cr up to 0.25 atoms per formula unit (a.p.f.u.). All other elements occur in small quantities (Table 3).

Sericite disseminated in mineralized metavolcaniclastic rocks is commonly associated with chlorite and carbonate patches. It contains higher FeO^t contents compared to sericite in listvenite and granitic rocks (Table 3). Na_2O contents in sericite are higher in the granitic rocks compared to that of sericite hosted in listvenite and metavolcaniclastic rocks. MgO contents are characteristically higher in sericite in listvenite. In the granitic rocks, sericite replaces feldspar and biotite, and is generally rich in Na and K. The phengite content of sericite (as measured by Mg + Fe a.p.f.u.) in altered granitic rocks is lower compared with sericites in listvenite and andesitic breccia/agglomerate. However, a general decrease in the phengite content in sericite is distinctly noticed in samples adjacent to the quartz lodes regardless the protolith lithology.

6.2. Chlorite

Chlorite is disseminated mainly in the sulfide-bearing wallrocks and less commonly dispersed in parts of the mineralized quartz veins. It occurs both as veins and as discrete flakes, often associated with sericite and carbonate, or as a replacement of ferromagnesian minerals in altered host rocks. Chlorites in each type of the altered host rocks have been subject to electron microprobe studies. Because chlorite forms commonly intimate aggregates with sericite and/or carbonate in most cases, analyses were selected using an arbitrary upper limit of 0.5 wt.% for total CaO + Na_2O + K_2O, following Hillier and Velde (1991).

According to the electron microprobe data, chlorites disseminated in the sulfide-bearing listvenite, volcanic breccia/agglomerate and granitic offshoots range between ripidolite and pycnochlorite. Cr-
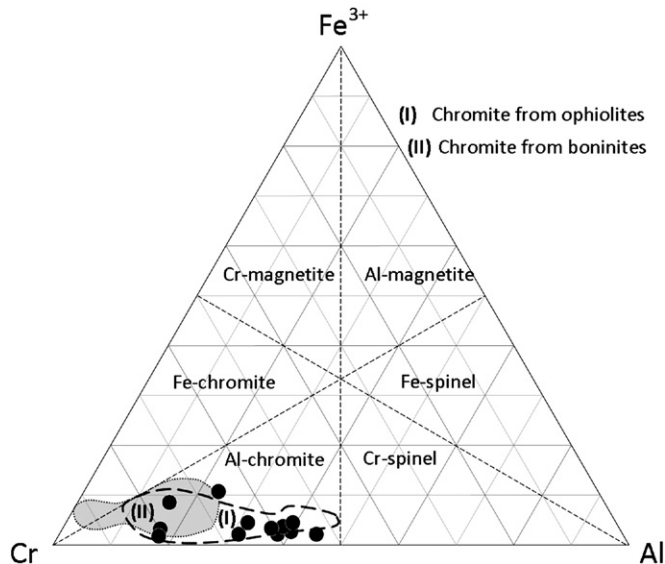

Fig. 7. Trivalent Cr–Al–Fe^{3+} ternary cation plot (after Stevens, 1944) of spinel grain cores from El-Anbat gold mine area showing the ophiolitic affinity of disseminated chromite grains. Fields are from Barnes and Roeder (2001).

Table 3
Representative EPMA data of sericite/fuchsite disseminated in mineralized listvenite, metavolcaniclastic and granitic rocks from the El-Anbat gold mine.

	Sericite in metavolcaniclastics					Sericite (fuchsite) in listvenite						Sericite in granite						
SiO$_2$	45.06	45.38	46.35	41.67	45.12	45.72	46.27	46.51	44.44	44.08	43.97	44.95	47.11	46.63	44.31	45.48	46.63	46.76
TiO$_2$	0.23	0.15	0.24	0.19	0.20	0.18	0.35	0.60	0.19	0.18	0.27	0.24	0.54	0.13	0.09	0.02	0.09	0.69
Al$_2$O$_3$	33.91	32.57	32.82	34.11	33.42	30.66	30.23	31.04	33.48	33.57	33.29	31.65	32.48	35.02	34.17	31.46	31.21	31.02
FeO	4.21	4.46	3.55	5.23	3.81	5.92	5.38	4.00	3.95	4.04	4.14	4.06	2.19	1.47	2.99	3.98	3.76	3.55
MnO	0.10	0.14	0.09	0.13	0.08	0.00	0.12	0.04	0.04	0.08	0.07	0.12	0.00	0.00	0.01	0.04	0.01	0.02
MgO	0.84	1.17	0.60	1.19	0.93	1.38	0.92	1.06	0.91	0.76	1.57	0.86	2.02	0.58	0.74	1.54	1.37	1.42
CaO	0.07	0.09	0.03	–	0.03	0.06	–	–	–	–	–	0.07	0.02	0.18	–	0.03	–	0.04
BaO	0.42	0.27	0.24	0.17	0.24	0.12	0.16	0.31	0.21	0.17	0.15	0.11	0.32	0.25	0.53	0.33	0.26	0.29
SrO	0.04	–	–	–	–	0.07	–	–	–	–	–	–	0.01	–	–	–	–	0.06
V$_2$O$_3$	0.08	0.06	0.05	–	–	0.23	0.04	0.05	–	–	0.02	0.00	0.08	–	–	–	0.10	0.09
Cr$_2$O$_3$	–	–	–	0.05	0.65	2.27	1.02	2.03	1.29	–	–	1.43	0.06	0.00	0.03	–	–	0.07
Na$_2$O	0.45	0.52	0.39	0.66	0.36	0.11	0.25	0.20	0.21	0.22	0.27	0.23	0.34	0.37	0.75	0.48	0.29	0.26
K$_2$O	9.23	9.59	10.33	10.59	10.02	7.40	9.02	8.66	10.11	9.94	10.49	9.38	9.96	9.26	10.32	11.02	11.53	9.34
Total	94.63	94.40	94.70	94.02	94.87	94.13	93.76	94.52	94.83	93.07	94.25	93.11	95.13	93.90	93.94	94.38	95.26	93.62
T$_2$	8.16	8.21	8.15	8.38	8.16	8.22	8.27	8.16	8.19	8.31	8.26	8.31	8.05	8.06	8.24	8.27	8.18	8.20
Formula based on 22 anions																		
Si	6.12	6.20	6.29	5.81	6.13	6.25	6.37	6.31	6.06	6.10	6.04	6.22	6.31	6.25	6.08	6.26	6.35	6.39
Ti	0.02	0.02	0.02	0.02	0.02	0.02	0.04	0.06	0.02	0.02	0.03	0.02	0.05	0.01	0.01	0.00	0.01	0.07
Al(iv)	1.88	1.80	1.71	2.19	1.87	1.75	1.63	1.69	1.94	1.90	1.96	1.78	1.69	1.75	1.92	1.74	1.65	1.61
Al(vi)	3.55	3.44	3.53	3.42	3.48	3.19	3.28	3.28	3.44	3.57	3.43	3.38	3.43	3.79	3.61	3.36	3.35	3.38
Al	5.43	5.24	5.25	5.61	5.35	4.94	4.90	4.97	5.38	5.47	5.39	5.16	5.13	5.54	5.53	5.10	5.01	4.99
Fe(ii)	0.48	0.51	0.40	0.61	0.43	0.68	0.62	0.45	0.45	0.47	0.48	0.47	0.25	0.16	0.34	0.46	0.43	0.41
Mn	0.01	0.02	0.01	0.02	0.01	0.00	0.01	0.00	0.00	0.01	0.01	0.01	0.00	0.00	0.00	0.00	0.00	0.00
Mg	0.17	0.24	0.12	0.25	0.19	0.28	0.19	0.21	0.19	0.16	0.32	0.18	0.40	0.12	0.15	0.32	0.28	0.29
Ca	0.01	0.01	0.00	0.00	0.00	0.01	0.00	0.00	0.00	0.00	0.00	0.01	0.00	0.03	0.00	0.00	0.00	0.01
Ba	0.02	0.01	0.01	0.01	0.01	0.01	0.01	0.02	0.01	0.01	0.01	0.01	0.02	0.01	0.03	0.02	0.01	0.02
Sr	0.00	0.00	0.00	0.00	0.00	0.01	0.00	0.00	0.00	0.00	0.00	0.00	0.00	0.00	0.00	0.00	0.00	0.00
V	0.01	0.01	0.00	0.00	0.00	0.03	0.00	0.01	0.00	0.00	0.00	0.00	0.01	0.00	0.00	0.00	0.01	0.01
Cr	0.00	0.00	0.00	0.01	0.07	0.25	0.11	0.22	0.14	0.00	0.00	0.16	0.01	0.00	0.00	0.00	0.00	0.01
Na	0.12	0.14	0.10	0.18	0.09	0.03	0.07	0.05	0.06	0.06	0.07	0.06	0.09	0.10	0.20	0.13	0.08	0.07
K	1.60	1.67	1.79	1.88	1.74	1.29	1.58	1.50	1.76	1.75	1.84	1.66	1.70	1.58	1.81	1.93	2.00	1.63
Total	14.00	14.06	14.00	14.39	14.05	13.78	13.91	13.81	14.07	14.05	14.19	13.95	13.96	13.80	14.15	14.22	14.17	13.88
XFe Fe/(Fe + Mg)	0.74	0.68	0.77	0.71	0.70	0.71	0.77	0.68	0.71	0.75	0.60	0.73	0.38	0.59	0.69	0.59	0.61	0.58
X$_{Ms}$	0.93	0.92	0.95	0.91	0.95	0.98	0.96	0.97	0.97	0.97	0.96	0.96	0.95	0.94	0.90	0.94	0.96	0.96

– below detection limit.

bearing, Mg-rich chlorite (wt.% MgO>FeO) is associated with serpentine minerals in listvenite. Petrographic relationships between this Mg-rich chlorite and primary relics of Cr-spinel crystals, as well as its significant Cr content (0.69–2.75 wt.%), suggest that this type of chlorite is originated from primary chrome spinels through hydrothermal alteration. Another chlorite type, in which wt.% FeO>MgO, is confined to quartz ± sericite and carbonate-rich domains in the mineralized listvenite. Although also Cr-bearing, this chlorite type has lesser contents of Cr (0.93–1.86) compared with the Mg-rich chlorite in a single sample. Chlorites in the granitic and metavolcaniclastic wallrocks and Fe-rich chlorites in listvenite show relatively high X_{Fe} (Fe/Fe + Mg + Mn = 0.37–0.49) values compared with the Mg-rich chlorite in listvenite (0.22–0.28), where Fe is calculated as total iron from microprobe analyses (Table 4).

Empirical calibrations for chlorite geothermometry have been proposed based on the tetrahedral Al occupancy and/or the octahedral vacancy as a function of measured temperatures in active geothermal systems and homogenization temperatures of fluid inclusions in fossil geothermal systems (e.g. Cathelineau, 1988; Cathelineau and Nieva, 1985; Hillier and Velde, 1991). However, many previous studies indicated that chlorite compositions are not only sensitive to prevailing physicochemical conditions but also to bulk rock composition (e.g., De caritat et al., 1993; Jowett, 1991; Kranidiotis and MacLean, 1987; Zang and Fyfe, 1995). In the present study, calculated temperatures based on Kranidiotis and MacLean (1987) geothermometer which is more appropriate for chlorites with X_{Fe}<0.5 (e.g., Frimmel, 1997). Interestingly, Fe-rich chlorites from the different altered wallrock types reveal a consistent temperature range (~300–340 °C), suggesting a unique hydrothermal stage. Calculations on Mg-rich chlorites in listvenite yielded, however, relatively lower temperatures (~270–290 °C), suggesting a possible different stage of chlorite formation (Table 4).

6.3. Carbonate

Carbonatization and pervasive sericitic (potassic) alteration, and silicification are widespread close to the mineralized shear zone and related quartz lodes. Carbonate minerals disseminated in the alteration zone vary according to the host rock lithology. Ankerite (ferroan dolomite) dominates in the altered listvenite and metavolcaniclastic rocks, whereas calcite as veinlets or replacement of biotite and/or associated with sericite is common in altered granitic rocks. Ankerite occurs as disseminated grains or forms network of veinlets in the mineralized wallrocks, generally in association with chlorite and abundant disseminated apatite. Ankerite has relatively uniform composition, with 33 to 57 mol% siderite component and traces of strontianite (SrCO$_3$). Manganese contents are generally low (<1 wt.% MnO). The widespread ankerite alteration in listvenite and metavolcaniclastic rocks has resulted in a substantial increase in loss-on-ignition (L.O.I.) and severe depletion in MgO concentration of altered rocks (Table 5). Calcite fills secondary fractures in the altered rocks and quartz veins. It is commonly associated with sericite and fine-grained comb (hydrothermal?) quartz grains. Iron and manganese contents are notably higher in calcite dispersed in the listvenite and metavolcaniclastic rocks compared to calcite in the altered granitic rocks (Table 5).

7. Geochemistry of the hydrothermally altered host rocks

Seventy-five samples of least- and most-altered host rocks, granitic offshoots and quartz veins were collected from the alteration/transpression zone at the El-Anbat mine area. Twenty-one samples were chosen for major- and trace-elements analysis using instrumental neutron activation analysis (INAA) and inductively coupled

Table 4

Representative EPMA data of chlorite disseminated in mineralized granitic offshoots, listvenite and metavolcaniclastic rocks from El-Anbat gold mine.

	Chlorite in granite					Chlorite in volcaniclastic breccias/agglomerates								Chlorite in listvenite												
														Mg-rich variety							Fe-rich variety					
SiO_2	27.02	26.78	26.43	25.52	26.05	27.16	26.90	26.50	27.12	26.83	27.17	26.75	26.48	28.46	28.34	28.14	27.78	28.80	27.46	27.03	26.05	26.55	25.68	25.80	25.22	26.97
TiO_2	0.03	0.10	0.03	0.07	0.08	0.07	0.04	0.07	0.09	0.14	0.09	0.06	0.14	0.07	0.05	–	0.04	0.03	0.07	0.01	0.04	0.01	0.00	0.00	0.03	0.05
Al_2O_3	20.07	21.59	21.38	22.16	21.13	20.58	21.84	21.19	20.80	20.75	20.41	21.42	21.51	17.32	19.63	19.44	19.65	20.70	18.95	19.69	21.52	20.68	22.18	21.54	22.30	21.01
FeO	22.04	21.64	22.36	20.55	23.87	21.94	22.72	20.10	21.66	23.27	21.87	22.96	23.42	15.65	13.42	12.84	14.52	13.58	14.21	15.41	20.08	20.87	22.90	22.38	24.45	21.84
MnO	0.28	0.20	0.22	0.24	0.13	0.15	0.14	0.30	0.14	0.11	0.20	0.12	0.13	0.12	0.16	0.17	0.11	0.20	0.11	0.09	0.07	0.04	0.05	0.02	0.03	0.00
MgO	18.42	17.92	18.04	17.58	16.31	16.79	17.31	18.82	17.38	17.08	17.63	16.34	16.83	23.02	23.98	24.72	22.65	24.09	22.88	23.22	18.25	18.19	15.97	15.06	14.46	13.69
CaO	0.05	0.04	–	0.07	0.06	0.07	0.02	0.06	0.07	0.11	0.26	0.04	0.01	–	0.02	0.01	0.06	0.03	0.06	0.02	0.04	0.04	0.14	0.03	0.11	0.02
BaO	–	0.01	–	0.04	0.01	–	–	0.04	–	–	–	0.04	–	–	–	0.07	0.00	–	–	0.00	0.01	0.00	0.03	0.01	0.07	0.00
SrO	–	–	–	–	–	–	–	–	–	–	–	–	–	–	–	0.01	0.05	–	0.07	0.04	0.01	0.02	0.02	0.02	0.01	0.04
V_2O_3	0.06	0.07	0.07	0.06	0.04	0.07	0.06	0.11	0.09	0.07	0.08	0.11	0.14	0.09	0.09	0.07	0.06	0.08	–	0.04	0.00	0.08	0.14	0.08	0.02	0.16
Cr_2O_3	0.04	0.05	0.05	0.00	0.01	0.03	0.02	0.08	0.02	0.05	0.01	–	0.01	1.22	0.61	1.13	2.00	0.66	2.39	2.75	0.93	1.16	1.50	1.86	1.01	1.38
Na_2O	0.03	0.06	0.02	0.02	0.00	0.04	–	0.03	–	0.05	0.02	0.03	0.00	–	–	0.02	–	0.03	0.01	0.04	0.03	0.02	0.02	0.03	0.10	0.02
K_2O	0.02	0.01	–	–	–	0.03	0.02	0.02	0.01	0.03	0.08	0.05	0.03	–	–	–	0.02	0.01	0.01	0.01	0.16	0.01	0.02	0.21	0.01	1.93
Total	88.07	88.49	88.60	86.31	87.71	86.94	89.07	87.38	87.96	88.50	87.82	87.93	88.70	85.95	86.30	86.64	86.94	88.22	86.24	85.36	87.19	87.67	88.66	87.05	87.84	87.12
T_2	12.38	12.27	12.31	12.55	12.54	12.50	12.23	12.42	12.31	12.38	12.39	12.43	12.35	12.31	12.07	12.02	12.11	11.79	12.23	12.50	12.41	12.39	12.39	12.61	12.60	12.65
Formula on basis of 28 oxygen																										
Si	5.57	5.47	5.42	5.33	5.44	5.65	5.48	5.45	5.60	5.53	5.60	5.53	5.44	5.83	5.69	5.63	5.60	5.65	5.59	5.62	5.38	5.47	5.30	5.42	5.29	5.68
Ti	0.00	0.02	0.00	0.01	0.01	0.01	0.01	0.01	0.01	0.02	0.01	0.01	0.02	0.01	0.01	0.00	0.01	0.00	0.01	0.00	0.01	0.00	0.00	0.00	0.00	0.01
$Al^{(iv)}$	2.43	2.53	2.58	2.67	2.56	2.35	2.52	2.55	2.40	2.47	2.40	2.47	2.56	2.17	2.31	2.37	2.40	2.35	2.41	2.38	2.62	2.53	2.70	2.58	2.71	2.32
$Al^{(vi)}$	2.44	2.66	2.58	2.78	2.64	2.70	2.72	2.59	2.67	2.57	2.57	2.75	2.66	2.01	2.34	2.22	2.27	2.44	2.13	1.72	2.60	2.50	2.69	2.74	2.80	2.89
Al	4.87	5.19	5.16	5.45	5.20	5.05	5.24	5.14	5.07	5.04	4.96	5.22	5.21	4.18	4.65	4.59	4.67	4.79	4.54	4.09	5.22	5.02	5.39	5.33	5.51	5.21
$Fe^{(ii)}$	3.80	3.69	3.83	3.59	4.17	3.82	3.87	3.46	3.74	4.01	3.77	3.97	4.03	2.68	2.25	2.15	2.45	2.23	2.42	2.68	3.47	3.60	3.95	3.93	4.29	3.84
Mn	0.05	0.03	0.04	0.04	0.02	0.03	0.02	0.05	0.02	0.02	0.03	0.02	0.02	0.02	0.03	0.03	0.02	0.03	0.02	0.02	0.01	0.01	0.01	0.00	0.01	0.00
Mg	5.66	5.45	5.51	5.47	5.08	5.21	5.25	5.78	5.35	5.25	5.42	5.04	5.16	7.03	7.18	7.38	6.81	7.05	6.94	7.20	5.62	5.59	4.91	4.71	4.52	4.30
Ca	0.01	0.01	0.00	0.02	0.01	0.02	0.00	0.01	0.02	0.02	0.06	0.01	0.00	0.00	0.00	0.00	0.01	0.01	0.01	0.00	0.01	0.01	0.03	0.01	0.02	0.00
Ba	0.00	0.00	0.00	0.00	0.00	0.00	0.00	0.00	0.00	0.00	0.00	0.00	0.00	0.00	0.00	0.01	0.00	0.00	0.00	0.00	0.00	0.00	0.00	0.00	0.01	0.00
Sr	0.00	0.00	0.00	0.00	0.00	0.00	0.00	0.00	0.00	0.00	0.00	0.00	0.00	0.00	0.00	0.00	0.01	0.00	0.01	0.00	0.00	0.00	0.00	0.00	0.00	0.00
V	0.01	0.01	0.01	0.01	0.01	0.01	0.01	0.02	0.01	0.01	0.01	0.02	0.02	0.01	0.01	0.01	0.01	0.01	0.00	0.01	0.00	0.01	0.02	0.01	0.00	0.03
Cr	0.01	0.01	0.01	0.00	0.00	0.00	0.00	0.01	0.00	0.01	0.00	0.00	0.00	0.20	0.10	0.18	0.32	0.10	0.38	0.45	0.15	0.19	0.24	0.31	0.17	0.23
Na	0.01	0.02	0.01	0.01	0.00	0.02	0.00	0.01	0.00	0.02	0.01	0.01	0.00	0.00	0.00	0.01	0.00	0.01	0.00	0.02	0.01	0.01	0.01	0.01	0.04	0.01
K	0.01	0.00	0.00	0.00	0.00	0.01	0.01	0.01	0.00	0.01	0.02	0.01	0.01	0.00	0.00	0.00	0.00	0.00	0.00	0.00	0.04	0.00	0.01	0.06	0.00	0.52
Total	19.99	19.92	19.99	19.93	19.94	19.82	19.89	19.96	19.84	19.93	19.91	19.85	19.92	19.96	19.92	19.98	19.90	19.89	19.93	20.10	19.94	19.92	19.87	19.79	19.87	19.83
XFe	0.40	0.40	0.41	0.40	0.45	0.42	0.42	0.37	0.41	0.43	0.41	0.44	0.44	0.28	0.24	0.23	0.26	0.24	0.26	0.27	0.38	0.39	0.45	0.45	0.49	0.47
$Al^{iv}c$	2.72	2.82	2.87	2.95	2.88	2.65	2.82	2.81	2.68	2.78	2.68	2.78	2.86	2.36	2.48	2.53	2.59	2.51	2.59	2.57	2.89	2.80	3.02	2.90	3.05	2.65
$T(°C)$	306	316	322	331	323	298	317	316	302	312	302	312	321	270	279	286	292	285	293	290	324	315	338	326	340	299

– below detection.

XFe = Fe/(Fe + Mg).

$Al^{iv}c$ (corrected tetrahedral Al), $T(°C)$ applying the equation $T = 106\ Al^{iv}c + 18$ according to Kranidiotis and MacLean (1987).

Table 5
Representative EPMA data of carbonate disseminated in mineralized granitic offshoots, listvenite and metavolcaniclastic rocks from El-Anbat gold mine.

	Calcite in granitic offshoot					Carbonate in metavolcaniclastic rocks				Carbonate in mineralized listvenite						
CaO	50.78	51.23	49.55	52.60	51.53	48.43	45.60	51.13	52.31	27.18	29.81	30.21	30.56	28.12	29.68	16.88
MgO	0.10	0.09	0.23	0.96	0.18	1.26	3.17	2.28	1.37	4.36	5.22	6.24	2.11	4.53	4.53	5.36
FeO	0.20	0.08	0.09	0.12	0.68	4.31	5.01	1.26	1.05	22.05	19.43	18.21	20.45	20.50	19.65	29.35
MnO	–	0.05	0.25	0.02	0.02	0.22	–	0.03	–	0.09	0.11	0.80	0.32	0.63	0.47	0.09
BaO	–	–	–	–	–	–	–	0.02	0.02	0.03	0.05	–	0.02	0.07	0.04	–
SrO	0.05	0.06	0.13	0.08	0.07	0.06	0.04	0.07	0.09	0.17	0.15	0.09	0.06	0.10	0.08	0.04
	51.13	51.51	50.25	53.78	52.48	54.28	53.82	54.79	54.84	53.88	54.77	55.55	53.52	53.95	54.42	51.72
Structural formulae basis on 6 oxygens, 2 cations																
Ca	1.99	1.99	1.97	1.96	1.96	1.78	1.69	1.87	1.91	1.01	1.09	1.09	1.14	1.04	1.09	0.65
Mg	0.00	0.00	0.01	0.04	0.01	0.05	0.12	0.08	0.05	0.16	0.19	0.22	0.08	0.17	0.17	0.21
Fe	0.01	0.00	0.00	0.00	0.03	0.16	0.19	0.05	0.04	0.82	0.71	0.66	0.76	0.76	0.72	1.13
Mn	0.00	0.00	0.01	0.00	0.00	0.01	0.00	0.00	0.00	0.00	0.00	0.03	0.01	0.02	0.02	0.00
Ba	0.00	0.00	0.00	0.00	0.00	0.00	0.00	0.00	0.00	0.00	0.00	0.00	0.00	0.00	0.00	0.00
Sr	0.00	0.00	0.01	0.00	0.00	0.00	0.00	0.00	0.00	0.01	0.01	0.00	0.00	0.00	0.00	0.00
sum	2.00	2.00	2.00	2.00	2.00	2.00	2.00	2.00	2.00	2.00	2.00	2.00	2.00	2.00	2.00	2.00
Mol%																
CaCO$_3$	99.32	99.46	98.61	97.81	98.19	89.22	84.73	93.31	95.39	50.45	54.43	54.38	57.10	52.13	54.53	32.64
MgCO$_3$	0.20	0.17	0.46	1.79	0.34	2.32	5.89	4.17	2.50	8.09	9.53	11.23	3.94	8.40	8.31	10.36
FeCO$_3$	0.39	0.16	0.18	0.22	1.30	7.94	9.31	2.30	1.91	40.93	35.48	32.78	38.21	38.00	36.10	56.75
MnCO$_3$	0.00	0.10	0.50	0.04	0.04	0.41	0.00	0.05	0.00	0.17	0.20	1.44	0.60	1.17	0.85	0.17
BaCO$_3$	0.00	0.00	0.00	0.00	0.00	0.00	0.00	0.04	0.03	0.06	0.09	0.00	0.04	0.13	0.06	0.00
SrCO$_3$	0.10	0.12	0.26	0.15	0.13	0.11	0.07	0.13	0.16	0.31	0.27	0.16	0.11	0.18	0.14	0.08
Sum	100.00	100.00	100.00	100.00	100.00	100.00	100.00	100.00	100.00	100.00	100.00	100.00	100.00	100.00	100.00	100.00
End members																
CaCO$_3$	98.63	98.91	97.21	95.61	96.38	78.45	69.45	86.62	90.78	0.90	8.86	8.77	14.20	4.25	9.05	0.00
CaMg(CO$_3$)$_2$	0.39	0.35	0.92	3.57	0.69	4.64	11.78	8.33	5.00	16.19	19.06	22.47	7.88	16.79	16.63	10.36
CaFe(CO$_3$)$_2$	0.78	0.31	0.36	0.45	2.59	15.88	18.62	4.60	3.83	81.86	70.95	65.56	76.42	76.00	72.20	56.75
CaMn(CO$_3$)$_2$	0.00	0.19	1.00	0.07	0.08	0.81	0.00	0.11	0.00	0.33	0.40	2.88	1.20	2.34	1.71	0.17
BaCO$_3$	0.00	0.00	0.00	0.00	0.00	0.00	0.00	0.08	0.06	0.11	0.18	0.00	0.07	0.26	0.13	0.00
SrCO$_3$	0.20	0.23	0.52	0.30	0.27	0.22	0.15	0.26	0.33	0.61	0.55	0.32	0.22	0.35	0.28	0.15
Sum	100.00	100.00	100.00	100.00	100.00	100.00	100.00	100.00	100.00	100.00	100.00	100.00	100.00	100.00	100.00	100.00
Ratios																
Fe#	0.667	0.471	0.281	0.111	0.791	0.774	0.612	0.356	0.434	0.835	0.788	0.745	0.906	0.819	0.813	0.846
Mg#	0.333	0.409	0.404	0.873	0.205	0.218	0.388	0.639	0.566	0.165	0.211	0.247	0.092	0.177	0.184	0.154

– below detection.

plasma-mass spectrometry (ICP-MS) methods, respectively, at the Activation Laboratories, Ancaster, Ontario (Table 6). Analytical precision is estimated to be better than 6 relative % for trace elements, and 3 relative % for major elements.

Based on the analytical data, it is apparent that significant changes in the chemical composition of the different host rocks types occurred during hydrothermal alteration (Table 6). The analyses indicate that gold is chiefly related to mineralized quartz veins (with up to 7.5 g/t Au) and to pervasively altered wallrocks (with traces to 5 g/t Au). Splays of the shear zones that cut the granitic masses are relatively heavily mineralized (ppm levels). The latter are found within the 10 to 20 m-wide central zone of the major transpressional zone. Boudinaged quartz veins cutting through highly strained host rocks characterize these heavily mineralized zones. Primary texture destruction and color bleaching combined with the geochemical data constrain on significant chemical/mineralogical changes during ore fluid infiltration into the sheared rocks. However, simple inspection of the geochemical analyses is not a satisfactory method for deducing complex processes in material transfer (e.g., Eilu et al., 2001). Instead, mass balance calculations can quantitatively define the components that were mobilized, and the style of geochemical dispersion.

Due to variation in the host rock lithology and considering additional igneous/metamorphic differentiation prior to hydrothermal alteration, the convenient methods of mass balance calculations (e.g., Grant, 1986, 2005; Gresens, 1967) cannot be appropriate in determining mass change in the El-Anbat gold deposit. The reason is that these methods do not consider any significant variation in the composition of the pre-

cursor rocks. Instead, the multiple-precursor method of MacLean and Barrett (1993) is used, because it considers the variation in pre-alteration composition of the host rocks. This method is based on the assumption Ti and Al behaved as immobile elements. Assuming constant Al_2O_3 and TiO_2 can be reasonable building on gold-related hydrothermal alteration post-dating listvenitization of ophiolites. This assumption is supported by the presence of intense alteration haloes around quartz veins, which cut the listvenized ophiolites, while alteration is weak at distance of the quartz veins. Concentrations of other low-mobility components such as P_2O_5 remain conserved, however TiO_2 and Al_2O_3 are more because of their higher and more accurately determined concentrations.

Mass balance calculations performed for samples collected from the various host rock types in El-Anbat mine are based on the immobility of Al and Ti (e.g., Barrett and MacLean, 1994; Eilu et al., 2001; Leitch and Lentz, 1994; MacLean and Kranidiotis, 1987). The immobility of Al and Ti is indicated by the coherent trends shown in the TiO_2 vs. Y, TiO_2 vs. V, Al_2O_3 vs. Y and Al_2O_3 vs. V diagrams (Fig. 8). Results of the mass balance calculations are summarized in Table 7. The results indicate that SiO_2, Fe_2O_3, CaO, K_2O, Na_2O, and volatile components (as loss on ignition, L.O.I.) are enriched in the altered rocks. Enrichments include also Au, Ag, Cu, As, Rb, Ba, Sb, W, Ce, La, and Sc. On the other side, Ni, V and Cr are apparently depleted in the altered rocks. The chemical changes represent carbonatization (gains in volatiles, CaO and Sr), sericitization (including replacement of Fe–Mg silicate and albite by sericite with gains in Ba, K, Rb, and loss in Na_2O and MgO). Gains in Fe_2O_3 can be attributed to ankerite veining and disseminated sulfides. Although V is

Table 6
Chemical composition of mineralized quartz lodes and least- and most-altered host rocks from the El-Anbat mine area.

	Listvenite					Metavolcaniclastic rocks								Granophyric offshoots					Quartz veins		
Wt.%	A-29*	A-17	A-9	A-32	A-36	A-28*	A-27	A-22	A-23	A-20	A-13	A-24	A-21	A-25*	A-7	A-30	A-6	A-10	A-16	A-12	A-19
SiO_2	38.89	42.60	41.08	39.72	47.92	64.36	65.03	67.15	65.34	65.28	68.08	64.77	69.14	73.59	76.16	74.48	73.05	70.63	94.51	96.17	92.50
TiO_2	0.28	0.13	0.22	0.24	0.15	0.34	0.28	0.18	0.32	0.21	0.17	0.22	0.16	0.18	0.11	0.10	0.14	0.15	0.06	0.01	0.02
Al_2O_3	3.08	2.49	2.78	3.03	2.59	15.44	13.63	13.97	14.02	12.51	12.67	12.73	12.03	11.77	11.23	10.84	11.06	11.22	1.03	0.71	1.51
Fe_2O_3	7.28	8.86	11.39	9.57	7.56	7.29	6.83	4.63	6.26	7.76	7.28	7.41	6.40	3.15	3.04	2.79	4.43	5.06	1.63	2.11	2.44
MnO	0.08	0.15	0.06	0.16	0.15	0.04	0.12	0.06	0.13	0.11	0.08	0.12	0.09	0.28	0.21	0.24	0.13	0.18	0.02	0.04	0.05
MgO	24.11	12.46	15.43	12.21	11.91	2.05	1.16	0.82	1.64	0.78	0.10	1.88	0.45	1.16	0.53	0.38	0.68	1.19	0.34	0.27	0.79
CaO	8.19	11.96	10.26	13.46	7.80	3.32	2.93	3.48	4.36	5.54	1.64	4.90	4.71	0.93	1.42	2.56	2.16	3.89	0.33	0.26	1.21
Na_2O	0.11	1.04	0.52	1.73	0.76	2.67	2.38	1.75	1.00	1.59	1.46	1.82	0.99	3.18	2.34	2.45	1.67	0.64	0.20	0.04	0.08
K_2O	0.41	0.98	1.90	3.53	2.36	2.42	3.19	4.19	3.85	3.75	4.94	3.43	3.89	2.73	2.96	4.18	3.32	3.32	0.37	0.23	0.68
P_2O_5	0.09	0.07	0.07	0.06	0.09	0.54	0.30	0.15	0.16	0.16	0.13	0.11	0.14	0.21	0.13	0.15	0.19	0.17	0.02	0.03	0.04
L.O.I.	16.89	18.49	16.11	15.39	17.91	2.13	2.01	3.20	3.08	2.52	3.52	3.37	2.67	2.33	2.71	2.32	3.23	3.80	0.58	0.54	0.14
SO_2	0.10	0.27	0.35	0.42	0.22	0.19	0.11	0.15	0.37	0.31	0.52	0.26	0.14	0.09	0.21	0.24	0.61	0.84	0.44	0.17	0.31
Total	99.52	99.50	100.2	99.51	99.41	100.8	97.98	99.72	100.5	100.5	100.6	101.1	100.8	99.60	101.1	100.7	100.6	101.1	99.08	100.4	99.45
Trace elements in ppm, Au in ppb																					
Au	26	121	671	1087	148	52	83	239	678	308	5180	5049	1738	–	1200	338	1940	14	7432	1332	1818
Ag	0.0	0.3	–	0.5	0.3	0.0	0.0	0.2	0.4	–	1.2	1.1	0.7	0.5	0.8	–	0.8	–	2.4	0.8	0.9
Cu	26	84	36	60	69	24	43	32	28	62	12	79	42	6	36	85	39	40	29	40	46
Cd	–	–	–	–	–	4.0	2.0	0.0	0.5	–	0.5	–	1.2	–	–	–	–	–	–	–	0.0
Pb	–	–	–	–	–	34	17	1	3	–	–	4	12	2	2	–	4	3	4	3	4
Ni	2066	2790	1244	1937	1965	25	46	45	25	66	4	90	45	4	38	14	18	38	56	58	69
Zn	50	115	50	117	98	102	85	50	73	104	50	131	89	30	143	133	92	76	16	42	45
As	36	153	411	506	220	25	51	267	360	198	899	804	538	106	532	226	637	108	979	456	742
Ba	121	209	180	330	240	565	247	243	670	730	740	643	616	94	450	400	540	390	–	–	179
Co	19	18	11	62	78	26	15	19	21	44	18	42	29	4	14	8	23	30	5	6	7
Cr	5429	4810	3413	4703	4657	52	19	253	236	200	179	270	180	9	10	21	19	16	130	215	62
Eu	0.6	0.4	0.5	0.5	0.7	0.7	0.9	1.2	1.8	1.3	1.4	0.9	1.2	1.4	2.0	0.9	1.9	1.8	–	–	–
Rb	7	15	18	20	16	24	39	26	47	39	23	36	22	32	45	52	61	79	9	5	11
Sb	0.5	2.5	6.2	8.4	5.6	0.0	0.5	1.1	2.3	1.2	4.3	3.5	2.9	1.2	3.4	0.9	2.5	0.5	6.1	3.2	3.8
Sc	4	12	15	8	13	10	6	14	19	23	16	9	15	4	8	6	9	12	3	1	2
Sr	222	276	284	172	192	153	32	168	139	244	198	235	178	221	101	242	140	55	19	64	68
V	59	37	54	45	44	121	88	72	88	69	66	81	59	85	51	47	59	63	34	27	34
W	1	2	4	9	2	1	2	6	8	5	11	10	9	7	11	4	9	0	6	4	5
Y	8	17	11	10	15	13	18	37	27	36	40	53	49	64	88	92	82	73	3	3	4
La	1.4	6.1	15.2	35.5	8.0	7.5	9.2	10.5	18.9	10.9	92.1	94.6	36.5	15.4	66.3	32.7	38.9	11.6	5.1	1.5	2.5
Ce	13	10	15	22	18	33	59	21	35	26	141	153	70	88	106	119	105	97	8	–	2
Nd	9	7	10	8	3	4	7	11	16	9	40	28	17	14	36	11	30	9	–	–	–
Sm	4.2	0.3	2.6	5.2	3.5	2.4	3.5	2.9	5.4	4.6	6.7	5.8	4.7	6.7	8.8	3.3	6.5	5.5	0.8	0.5	0.7
Yb	1.9	0.6	1.2	3.1	2.6	1.7	2.2	2.5	3.1	2.6	3.8	2.9	2.8	0.9	5.8	1.4	2.8	4.6	0.5	0.4	0.5
Lu	0.06	0.07	0.09	0.04	0.05	0.22	0.21	0.27	0.25	0.31	0.34	0.26	0.31	0.45	0.24	0.30	0.47	0.48	–	–	–
3 K/Al	0.40	1.18	2.05	3.50	2.73	0.47	0.70	0.90	0.82	0.90	1.17	0.81	0.97	0.70	0.79	1.16	0.90	0.89	1.08	0.97	1.35

*least-altered samples, – below detection limit.

consistently depleted in the altered rocks, Cr is leached from the listvenite and enriched in the metavolcaniclastic and granophyric rocks. Similarly, Ni and Co show erratic variation, likely as a result of variable amounts of disseminated Ni–Fe–As sulfides in the host rocks. Chemical changes suggest alteration indices that are potentially useful at El-Anbat gold deposit should be based on S, K_2O, CaO, Rb, Sr, V, and Y as these components show extensive mobility. The sericitization index (3 K/Al, molar ratio; Kishida and Kerrich, 1987) is distinctly higher in altered rocks compared to least-altered rocks. The increase in the L.O.I., S, and CaO in the mineralized host rocks is consistent with the pervasive carbonatization and sulfidization of the sheared rocks.

Results of mass balance calculations suggest that gold and related pathfinders (e.g., Au, S, Ag, As, Sb, and W) are generally enriched throughout the alteration zone. As enrichment of these elements propositionally correlate with S contents in the analyzed samples (Table 8), sulfidation of the host rocks could have been vital in the disseminated mineralization. The mass balance results reveal that Au, S, Ag, As, Sb, and W show no differences in their mobility relative to the different host rock lithologies. Therefore, concentrations of these pathfinder elements can be directly used as indicators of Au dispersion.

8. Discussion

The El-Anbat gold deposit shows geological characteristics that classify orogenic gold deposits, including metamorphosed host rocks, low sulfide minerals content, typical alteration assemblages and a spatial association with transpressional structures (cf. Groves et al., 1998). Structural control on mineralization is evident at the mine, and can be extrapolated to a regional scale. Foliation deflection could have produced sites of local dilation during D2 deformation (compression along a WSW–ENE axis) and enhanced fluid flow. Development of narrow shear zones at contacts between sheets of listvenite and metavolcaniclastic rocks could have facilitated fluid infiltration. It might also be assumed that foliation intersection was either a zone of high permeability during D2, or that D2 ore shoots were reoriented together with remobilization of gold. Several shear zones are intimately associated with the lenticular granitic bodies, which may suggest that the high-strain zones have nucleated and propagated along lithological contacts. Therefore, the crustal continuum model for 'gold-only' deposits, which follows a deep-seated fluid source and a single-pass migration along crustal-scale fault zones (e.g., Colvine, 1989; Groves, 1993; Groves et al., 1992; Ridley and Diamond, 2000), can explain the genesis of gold mineralization at the El-Anbat mine.

The relationship between gold mineralization and the abundant granitic offshoots in the mine area and along the shear zones is not clear. However, occurrence of the ore bodies and related sulfide-bearing alteration zones along the transpression zone along with boudinaged granitic bodies may indicate a possible hydrothermal activity concomitant with emplacement of the granitic offshoots (e.g., Mueller et al., 1996). This assumption is verified by geochemical
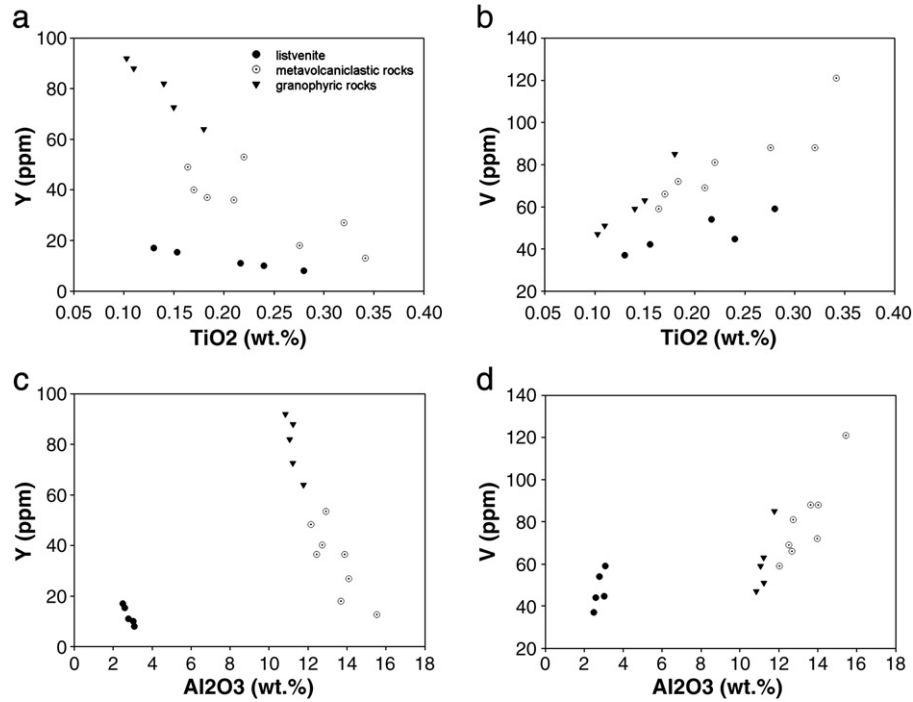
Fig. 8. Two-element variation diagrams for potentially immobile elements determined for samples of least- and most-altered host rocks from the El-Anbat gold mine. Notice the similar fractionation trends when plotting the same element versus TiO$_2$ and Al$_2$O$_3$, respectively. Symbols in b, c and d are as in a.

Table 7
Hydrothermal alteration-induced mass gains and losses in the El-Anbat gold deposit.

g/100 g	A-17	A-9	A-32	A-36	An_27	A_22	A-23	A-20	A-13	A-24	A-21	A-7	A-30	A-6	A-10
SiO$_2$	7.01	4.82	2.80	6.81	4.73	6.22	4.82	4.50	7.20	7.67	11.44	5.90	3.30	2.66	0.67
TiO$_2$	−0.14	−0.05	−0.03	−0.13	−0.05	−0.15	0.00	−0.12	−0.16	−0.10	−0.16	−0.07	−0.07	−0.03	−0.02
Al$_2$O$_3$	−0.40	−0.12	0.10	−0.61	−0.96	−0.76	−0.60	−2.24	−2.12	−1.28	−2.25	−0.05	−0.58	−0.23	0.03
Fe$_2$O$_3$	2.27	4.84	2.76	−0.07	−0.03	−2.43	−0.67	0.89	0.36	0.95	−0.28	0.03	−0.26	1.48	2.17
MnO	0.08	−0.02	0.09	0.06	0.08	0.02	0.10	0.08	0.04	0.09	0.06	−0.06	−0.03	−0.14	−0.09
MgO	−10.68	−7.69	−11.30	−12.75	−0.83	−1.19	−0.32	−1.24	−1.95	0.04	−1.56	−0.60	−0.77	−0.45	0.09
CaO	4.70	2.73	5.93	−0.75	−0.21	0.33	1.30	2.52	2.13	1.84	1.84	0.55	1.71	1.33	3.16
Na$_2$O	1.01	0.44	1.71	0.61	−0.14	−0.84	−1.62	−0.99	−1.14	−0.65	−1.59	−0.74	−0.65	−1.44	−2.51
K$_2$O	0.65	1.62	3.29	1.84	0.97	1.99	1.66	1.54	2.77	1.40	1.84	0.36	1.58	0.73	0.76
P$_2$O$_5$	−0.01	−0.01	−0.03	−0.01	−0.22	−0.38	−0.38	−0.37	−0.40	−0.42	−0.38	−0.08	−0.06	−0.01	−0.03
L.O.I.	3.04	0.25	−0.74	0.19	0.01	1.23	1.13	0.53	1.57	1.62	0.80	0.49	0.06	1.03	1.66
SO$_2$	0.20	0.29	0.32	0.12	−0.07	−0.03	0.21	0.14	0.37	0.10	−0.03	0.13	0.16	0.54	0.78
g/1000 kg															
Au	104	689	1115	116	36	199	665	273	5393	5563	1853	1252	349	2025	15
Ag	0.3	–	0.5	0.3	-	0.2	0.4	–	1.3	1.2	0.8	0.3	−0.5	0.3	−0.5
Cu	64	12	37	40	21	10	5	41	−12	63	22	32	82	35	361
Cd	–	–	–	–	−1.9	−4.0	−3.5	–	−3.5	–	−2.7	–	–	–	–
Pb	–	–	–	–	−15.9	−32.5	−30.7	–	–	−29.4	−20.2	0.1	-	2.2	1.2
Ni	940.6	−742.4	−32.8	−192.1	23.2	22.4	1.5	44.3	−21.1	74.8	24.3	35.9	10.5	14.8	36.0
Zn	73.9	3.2	72.4	43.8	−11.4	−49.2	−24.8	8.0	−49.2	44.3	−3.9	119.3	106.9	66.0	49.9
As	129.0	401.4	495.1	173.5	29.6	256.1	356.4	183.5	919.9	869.0	564.5	445.2	124.1	554.8	107.9
Ba	104.2	70.5	225.3	107.9	−301.8	−308.8	144.8	205.5	213.3	150.9	110.5	375.5	318.7	469.4	315.8
Co	0.4	−6.9	46.4	55.4	−9.9	−5.7	−3.8	20.7	−6.8	21.4	6.2	10.6	4.3	20.0	27.5
Cr	−245.6	−1798.1	−493.5	−987.5	−31.1	213.9	198.1	159.3	136.4	248.2	146.0	1.4	12.7	10.8	7.8
Eu	−0.2	−0.1	−0.1	0.1	0.3	0.6	1.2	0.7	0.8	0.3	0.7	0.7	−0.5	0.6	0.5
Rb	9.2	12.2	14.3	8.3	17.4	3.3	25.4	17.1	0.2	16.0	−0.2	15.0	21.7	31.7	51.1
Sb	2.2	6.1	8.3	4.8	0.5	1.2	2.5	1.3	4.5	3.9	3.2	2.3	−0.3	1.4	−0.7
Sc	8.3	11.6	4.3	7.5	−3.1	4.9	10.3	14.2	7.2	−0.1	6.9	4.2	2.1	5.3	8.3
Sr	75.4	80.5	−41.1	−39.2	−119.0	23.9	−5.8	104.4	55.5	108.7	42.1	−115.1	29.3	−74.4	−162.7
V	−19.1	−1.5	−12.1	−17.0	−27.5	−45.3	−27.8	−48.2	−51.6	−30.9	−56.3	−31.8	−36.5	−23.4	−18.8
W	1.2	3.3	8.4	0.9	1.1	5.3	7.5	4.3	10.6	10.1	8.9	4.5	−2.9	2.4	−7.0
Y	10.3	3.7	2.5	6.6	6.1	25.9	15.6	25.0	29.0	45.9	40.7	27.9	31.0	21.6	12.3
La	5.2	14.7	35.9	6.2	2.3	3.5	12.5	4.0	97.7	89.3	32.6	53.8	18.4	25.2	−3.2
Ce	−2.2	3.0	10.1	4.2	29.6	−11.1	4.3	−5.7	115.1	136.6	43.8	22.6	37.7	20.2	14.0
Nd	−1.5	1.6	−0.6	−6.1	2.9	7.6	12.9	5.5	38.0	26.8	14.8	23.6	−2.6	17.3	−4.5
Sm	−3.9	−1.4	1.3	−0.9	1.3	0.6	3.3	2.5	4.6	4.1	2.7	2.5	−3.3	0.1	−0.9
Yb	−1.3	−0.6	1.3	0.6	0.6	0.9	1.6	1.0	2.3	1.5	1.4	5.2	0.5	2.0	3.9
Lu	0.02	0.03	−0.02	−0.01	0.00	0.06	0.04	0.11	0.14	0.07	0.12	−0.20	−0.14	0.04	0.05

– not determined.

Table 8
Correlation coefficients between gold, sulfur and pathfinders at El-Anbat gold deposit.

	Au	Ag	As	Sb	W
S	0.25	0.48	0.3	0.22	0.08
Au		0.93	0.89	0.45	0.55
Ag			0.84	0.46	0.52
As				0.64	0.65
Sb					0.41

analyses that indicate anomalous concentrations of gold (ppb levels) in zones of altered host rocks far-removed (meters to tens of meters) from the quartz lodes. Mass balance calculations of the El-Anbat gold deposit suggest that infiltrated hydrothermal fluids under brittle-ductile shear conditions led to addition of Au, As, Cu, and Sb, likely concomitant with silicification, sulfidation and sericitization of the host rocks (see Table 7). Marked coherence between As, Sb, and Au is evident in practically all types of gold deposits (e.g., Boyle and Garrett, 1970; Hill, 1980). These pathfinder elements can potentially be used to define target areas that are much larger than the mappable alteration halo (e.g., Eilu and Mikucki, 1998).

Results of the electron microprobe analyses and geochemical dispersion reveal that gold is mostly associated with S–As mineral phases (As-pyrite, arsenopyrite, and gersdorffite) throughout the alteration zone. Free-milling in secondary sites (e.g., micro-crakes) may point toward mobilization of refractory gold from early pyrrhotite in carbonatized serpentinite, which led to increased gold grade in the highly silicified zones. Pentlandite and Ni-bearing minerals formed either at earlier/high temperature stages of the hydrothermal alteration or might pre-date mineralization and un-related to the gold-ore fluids. If the second assumption applies, alteration of pyrrhotite may have liberated additional Au into the mineralizing fluids (e.g., Bonnemaison and Marcoux, 1990).

9. Conclusions

The El-Anbat gold deposit is related to extensive, transpression-related shear zones that generally follow lithological competency contrasts within a back-arc ophiolitic mélange and underlying island arc metavolcaniclastic rocks. Development of these shear zones is likely related to the Wadi Kharit–Wadi Hodein shear system (analog of the 655–540 Ma, Najd strike–slip fault system in the Eastern Desert of Egypt; Greiling et al., 1994). Syn-deformation genesis of the gold-bearing lodes is evident from the lode geometry, stretching lineations on vein walls and variable quartz textures.

Geochemical studies reveal that low-grade zones (ppb levels) of gold mineralization occur in the highly-deformed serpentinite and metavol-caniclastic rocks, whereas, shears that coincide with the granitic offshoots in the middle of the NNW-transpressional corridor are heavily mineral-ized (ppm levels). Dispersion of gold and related pathfinders (i.e., As and Sb) has been reported far beyond the lode zone in the El-Anbat mine area. Compared to the quartz lode systems that have traditionally been the mining target, the volume of potential ore may be greater if alteration zones are considered. Similarly, other Najd-related transpressional zones in the Eastern Desert of Egypt can be potential for gold especially those cut through ophioltic mélange rocks. Prospective areas along these transpres-sional zones are very likely where narrow, localized, high-strain splays stitching competent granitic offshoots or intrusions.

Acknowledgements

References

Abdeen, M.M., Sadek, M.F., Greiling, R.O., 2008. Thrusting and multiple folding in the Neoproterozoic Pan-African basement of Wadi Hodein area, south Eastern Desert, Egypt. Journal of African Earth Sciences 52 (1–2), 21–29.

Abdelsalam, M.G., Abdeen, M.M., Dowaidar, H.M., Stern, R.J., Abdelghaffar, A.A., 2003. Structural evolution of the Neoproterozoic Western Allaqi–Heiani suture, south-eastern Egypt. Precambrian Research 124, 87–104.

Abdelsalam, M.G., Stern, R.J., 1996. Sutures and shear zones in the Arabian–Nubian Shield. Journal of African Earth Sciences 23, 289–310.

Abd El-Wahed, M.A., Kamh, S.Z., 2010. Pan-African dextral transpressive duplex and flower structure in the Central Eastern Desert of Egypt. Gondwana Research 18 (2–3), 315–336.

Barnes, S.J., Roeder, P.L., 2001. The range of spinel compositions in terrestrial mafic and ultramafic rocks. Journal of Petrology 42, 2279–2302.

Barrett, T.J., MacLean, W.H., 1994. Chemostratigraphy and hydrothermal alteration in exploration for VHMS deposits in greenstones and younger volcanic rocks. In: Lenz, D.R. (Ed.), Alteration and Alteration Processes Associated with Ore-forming Systems: Geological Association of Canada, Short Course Notes, 11, pp. 433–467.

Berhe, S.M., 1990. Ophiolites in northeast and east Africa: implication for Proterozoic crustal growth. Journal of the Geological Society of London 147, 41–57.

Bierlein, F.P., Crowe, D.E., 2000. Phanerozoic orogenic lode gold deposits. Reviews in Economic Geology 13, 103–139.

Bonnemaison, M., Marcoux, E., 1990. Auriferous mineralization in some shear-zones: a three-stage model of metallogenesis. Mineralium Deposita 25 (2), 96–104.

Botros, N.S., 1993. The possible occurrence of placer gold in areas lacking quartz veins in Egypt. Journal of Geochemical Exploration 49, 287–290.

Boyle, R.W., Garrett, R.G., 1970. Geochemical prospecting — a review of its status and future. Earth Science Reviews 6, 51–75.

Bregar, M., Fritz, H., Unzog, W., 1997. Structural evolution of low-angle normal faults SE of the Gebel El Sibai crystalline dome; Eastern Desert, Egypt: evidence from palaeopiezometry and vorticity analysis. Zentralblatt fuer Geologie und Palaeonto-logie 3 (4), 243–256.

Cathelineau, M., 1988. Cation site occupancy in chlorites and illites as a function of temperature. Clay Minerals (London) 23, 471–485.

Cathelineau, M., Nieva, D., 1985. A chlorite solid solution geothermometer. The Los Azufres (Mexico) geothermal system. Contributions to Mineralogy and Petrology 91, 235–244.

Cole, J.C., Hedge, C.E., 1986. Geochronologic investigation of Late Proterozoic rocks in the northeastern Shield of Saudi Arabia, scale 1:1,000,000. Technical Record USGS-TR-05-5. Saudi Arabian Deputy Ministry for Mineral Resources.

Colvine, A.C., 1989. An empirical model for the formation of Archean gold deposits: products of final cratonization of the Superior Province, Canada. In: Keays, R.R. (Ed.), The Geology of Gold Deposits: Economic Geology Monographs, 6, pp. 37–53.

Cox, S.F., Wall, V.J., Etheridge, M.A., Potter, T.F., 1991. Deformational and metamorphic processes in the formation of mesothermal vein-hosted gold deposits—examples from the Lachlan Fold Belt in central Victoria, Australia. Ore Geology Reviews 6, 391–423.

De Caritat, P., Hutcheon, I., Walsche, J.L., 1993. Chlorite geothermometry: a review. Clays and Clay Minerals 41, 219–239.

de Wall, H., Greiling, R.O., Fouad Sadek, M., 2001. Post-collisional shortening in the late Pan-African Hamisana high strain zone, SE Egypt; field and magnetic fabric evidence. Precambrian Research 107, 179–194.

Eilu, P., Mikucki, E.J., 1998. Alteration and primary geochemical dispersion associated with the Bulletin lode-gold deposit, Wiluna, Western Australia. Journal of Geochemical Exploration 63, 73–103.

Eilu, P., Mikucki, E.J., Dugdale, A.L., 2001. Alteration zoning and primary geochemical dispersion at the Bronzewing lode-gold deposit, Western Australia. Mineralium Deposita 36 (1), 13–31.

El-Dougdoug, A., 1990. Gold anomalies in the Late Proterozoic felsic/mafic volcanose-dimentary sequence and associated rocks, Gebel Abu Marawat area, Eastern Desert, Egypt. Bulletin of the Faculty of Science, Cairo University 58, 533–548.

El-Gaby, S., List, F.K., Tehrani, R., 1988. Geology, evolution and metallogenesis of the Pan-African Belt in Egypt. In: El-Gaby, S., Greiling, R.O. (Eds.), The Pan-African belt of Northeast Africa and Adjacent Area Friedr Viewegsohn, Braunschweig/Wiesbaden, pp. 17–68.

El-Mezayen, A.M., Hassaan, M.M., El-Hadad, M., Hassanein, M.M., 1995. Petrography, geochemistry and ore microscopy of Abu Marawat metavolcanics and associated gold mineralisation, North Eastern Desert, Egypt. Bulletin of the Faculty of Science, Al-Azhar University 6 (2), 1999–2021.

Fialin, M., Rémy, H., Richard, C., Wagner, Ch., 1999. Trace element analysis with the electron microprobe: new data and perspectives. American Mineralogist 84, 70–77.

Fowler, A.R., El Kalioubi, B., 2004. Gravitational collapse origin of shear zones, foliations and linear structures in the Neoproterozoic cover nappes, Eastern Desert, Egypt. Journal of African Earth Sciences 38, 23–40.

Frimmel, H.E., 1997. Chlorite thermometry in the Witwatersrand Basin: constrains on the Paleoproterozoic geotherm in the Kaapvaal Craton, South Africa. Journal of Geology (Chicago) 105, 601–615.

Fritz, H., Wallbrecher, E., Khudeir, A.A., Abu el Ela, F., Dallmeyer, D.R., 1996. Formation of Neoproterozoic metamorphic core complexes during oblique convergence (Eastern Desert, Egypt). Journal of African Earth Sciences 23, 311–329.

Goldfarb, R.J., Baker, T., Dube, B., Groves, D.I., Hart, C.J., Gosselin, P., 2005. Distribution, character and genesis of gold deposits in metamorphic terranes. In: Hedenquist, J.W., Thompson, J.F.H., Goldfarb, R.J., Richards, J.P. (Eds.), Economic Geology 100th Anniversary Volume, pp. 407–450.

Grant, J.A., 1986. The isocon diagram: a simple solution to Gresens' equation for metasomatic alteration. Economic Geology 81, 1976–1982.

Grant, J.A., 2005. Isocon analysis: a brief review of the method and applications. Physics and Chemistry of the Earth, Parts A/B/C 30 (17–18), 997–1004.

Greiling, R.O., Abdeen, M.M., Dardir, A.A., El Akhal, H., El Ramly, M.F., Kamal El Din, G.M., Osman, A.F., Rashwan, A.A., Rice, A.H.N., Sadek, M.F., 1994. A structural synthesis of the Proterozoic Arabian–Nubian Shield in Egypt. Geologische Rundschau 83, 484–501.

Gresens, R.L., 1967. Composition–volume relationships of metasomatism. Chemical Geology 2, 47–55.

Groves, D.I., 1993. The crustal continuum model for late-Archaean lode-gold deposits of the Yilgarn Block, Western Australia. Mineralium Deposita 28, 357–387.

Groves, D.I., Barley, M.E., Barnicoat, A.C., Cassidy, K.F., Fare, R.J., Hagemann, S.G., Ho, S.E., Hronsky, J.M.A., Mikucki, E.J., Mueller, A.G., McNaughton, N.J., Perring, C.S., Ridley, J.R., Vearncombe, J.R., 1992. Sub-greenschist to granulite-hosted Archaean lode–gold deposits of the Yilgarn Craton; a depositional continuum from deep-sourced hydrothermal fluids in crustal-scale plumbing systems. In: Glover, J.E., Ho, S.E. (Eds.), The Archaean; Terrains, Processes and Metallogeny. : Proceedings Volume for the Third International Archaean Symposium, 22. Geology Department and Extension Service, University of Western Australia, pp. 325–337.

Groves, D.I., Goldfarb, R.J., Gebre-Mariam, M., Hagemann, S.G., Robert, F., 1998. Orogenic gold deposits: a proposed classification in the context of their crustal distribution and relationship to other gold deposit types. Ore Geology Reviews 13, 7–27.

Halls, C., Zhao, R., 1995. Listvenite and related rocks: perspectives on terminology and mineralogy with reference to an occurrence at Cregganbaun, Co. Mayo, Republic of Ireland. Mineralium Deposita 30, 303–313.

Hassaan, M.M., El Mezayen, A.M., Dardir, A.A., Hassanein, M.M., 1996. Primary distribution pattern of gold and associated elements in Abu Marawat mine, North Eastern Desert and significance to exploration. Al-Azhar Bulletin of Science 7 (1), 995–1016.

Hassaan, M.M., Ramadan, T.M., Abu El Leil, I., Sakr, S.M., 2009. Lithochemical surveys for ore metals in arid region, Central Eastern Desert, Egypt: using Landsat ETM+ imagery. Australian Journal of Basic and Applied Sciences 3, 512–528.

Hill, M., 1980. Costerfield Au-Sb prospect, Melbourne Trough, Vic. In: Butt, C.R.M., Smith, R.E. (Eds.), Conceptual Models in Exploration Geochemistry: Journal of Geochemical Exploration, pp. 304–306.

Hillier, S., Velde, B., 1991. Octahedral occupancy and the chemical composition of diagenetic (low-temperature) chlorites. Clay Minerals 26, 149–168.

Jercinovic, M.J., Williams, M.L., 2005. Analytical perils (and progress) in electron microprobe trace element analysis applied to geochronology: background acquisition, interferences, and beam irradiation effects. American Mineralogist 90, 526–546.

Jowett, E.C., 1991. Fitting iron and magnesium into the hydrothermal chlorite geothermometer. GAC/MAC/SEG Joint Annual Meeting (Toronto): Program with Abstracts, 16, p. A62.

Kamenetsky, V.S., Crawford, A.J., Meffre, S., 2001. Factors controlling chemistry of magmatic spinel: an empirical study of associated olivine, Cr-spinel and melt inclusions in primitive rocks. Journal of Petrology 42, 655–671.

Kishida, A., Kerrich, R., 1987. Hydrothermal alteration zoning and gold concentration at the Kerr-Addison Archean lode gold deposit, Kirkland Lake, Ontario. Economic Geology 82, 649–690.

Kranidiotis, P., MacLean, W.H., 1987. The systematics of chlorite alteration at the Phelps Dodge massive sulfide deposit, Matagami, Quebec. Economic Geology 82, 1898–1911.

Kretschmar, U., Scott, S.D., 1976. Phase relations involving arsenopyrite in the system Fe–As–S and their application. The Canadian Mineralogist 14, 364–386.

Kröner, A., Greiling, R., Reischmann, T., Hussein, I.M., Stern, R.J., Durr, S., Kruger, J., Zimmer, M., 1987. Pan-African crustal evolution in northeast Africa. In: Kröner, A. (Ed.), Proterozoic Lithospheric Evolution: American Geophysical Union, Geodynamic Series, 17, pp. 235–257.

Leitch, C.H.B., Lentz, D.R., 1994. The Gresens approach to mass balance constraints of alteration systems: methods, pitfalls, examples. In: Lenz, D.R. (Ed.), Alteration and Alteration Processes Associated with Ore-forming Systems: Geological Association of Canada, Short Course Notes, 11, pp. 161–192.

Li, X., Kwak, T.A.P., Brown, R.W., 1998. Wallrock alteration in the Bendigo gold ore field, Victoria, Australia: uses in exploration. Ore Geology Reviews 13, 381–406.

MacLean, W.H., Kranidiotis, P., 1987. Immobile elements as monitors of mass transfer in hydrothermal alteration: Phelps Dodge massive sulphide deposits, Matagami, Quebec. Economic Geology 82, 951–962.

MacLean, W.H., Barrett, T.J., 1993. Lithogeochemical techniques using immobile elements. Journal of Geochemical Exploration 48, 109–133.

Mueller, A.G., Campbell, I.H., Schiotte, L., Sevigny, J.H., Layer, P.W., 1996. Constraints on the age of granitoid emplacement, metamorphism, gold mineralization, and

subsequent cooling of the Archean greenstone terrane at Big Bell, Western Australia. Economic Geology 91, 896–915.

Nano, L., Kontny, A., Sadek, M.F., Greiling, R.O., 2002. Structural evolution of metavolcanics in the surrounding of the gold mineralization at El Beida, South Eastern Desert, Egypt. Annals Geological Survey of Egypt 25, 11–22.

Osman, A., 1995. The mode of occurrence of gold-bearing listvenite at El Barramiya gold mine, Eastern Desert, Egypt. Middle East Research Centre. Ain Shams University. Earth Sciences Series 9, 93–103.

Rajlich, P., 1993. Riedel shear: a mechanism for crenulation cleavage. Earth Science Reviews 34, 167–195.

Ramadan, T.M., 1995. Geological and geochemical studies on some basement rocks at Wadi Hodein area, South Eastern Desert, Egypt. PhD. Thesis, Al Azhar University, Cairo, p. 184.

Ramadan, T.M., 2002. Exploration for gold-bearing listwaenites at Um Khasila area, Central Eastern Desert, Egypt. Egyptian Journal of Remote Sensing and Space Sciences 5, 63–76.

Ramadan, T.M., Kontny, A., 2004. Mineralogical and structural characterization of alteration zones detected by orbital remote sensing at Shalatein District area, SE Desert, Egypt. Journal of African Earth Sciences 40, 89–99.

Ramadan, T.M., Sadek, M.F., Abu El Leil, I., Salem, S.M., 2005. Um El Touyur El Fuqani gold mineralization, South Eastern Desert, Egypt: using Landsat ETM+ IMAGERY. Annals of the Geological Survey of Egypt 28, 263–281.

Ridley, J.R., Diamond, L.W., 2000. Fluid chemistry of orogenic lode gold deposits and implications for genetic models. Reviews in Economic Geology 13, 141–162.

Rieder, M., Cavazzini, G., D'yakonov, Yu.S., Frank-Kamenetskii, V.A., Gottardi, G., Guggenheim, S., Koval, P.V., Mueller, G., Neiva, A.M.R., Radoslovich, E.W., Robert, J.L., Sassi, F.P., Takeda, H., Weiss, Z., Wones, D.R., 1999. Nomenclature of the micas. Mineralogical Magazine 63 (2), 267–279.

Robinson, B.W., Ware, N.G., Smith, D.G.W., 1998. Modern electron-microprobe trace-element analysis in mineralogy. In: Cabri, L.J., Vaughan, D.J. (Eds.), Modern Approaches to Ore and Environmental Mineralogy: Mineralogical Association of Canada, Short Course, 27, pp. 153–180.

Savage, J.C., Svarc, J.L., Prescott, W.H., Murray, M.H., 2000. Deformation across the forearc of the Cascadia subduction zone at Cape Blanco, Oregon. Journal of Geophysical Research 105, 3095–3102.

Sibson, R.H., Robert, F., Poulsen, K.H., 1988. High-angle reverse faults, fluid-pressure cycling, and mesothermal gold-quartz deposits. Geology 16, 551–555.

Stacey, J.S., Agar, R.A., 1985. U-Pb isotopic evidence for the accretion of a continental micro-plate in the Zalm region of the Saudi Arabian Shield. Journal of the Geological Society of London 142, 1189–1203.

Stern, R.J., 1985. The Najd Fault system, Saudi Arabia and Egypt: a late Precambrian rift-related transform system? Tectonics 4, 497–511.

Stern, R.J., 1994. Arc assembly and continental collision in the Neoproterozoic East African orogen: implications for the consolidation of Gondwanaland. Annual Reviews in Earth and Planetary Sciences 22, 319–351.

Stern, R.J., Hedge, C.E., 1985. Geochronologic and isotopic constraints on late Precambrian crustal evolution in the Eastern Desert of Egypt. American Journal of Science 285, 97–127.

Stern, R.J., Kröner, A., Rashwan, A.A., 1991. A Late Precambrian (710 Ma) high vulcanicity rift in the south Eastern Desert of Egypt. Geologische Rundschau 80, 155–170.

Stern, R.J., Nielsen, K.C., Best, E., Sultan, M., Arvidson, R.E., Kröner, A., 1990. Orientation of late Precambrian sutures in the Arabian–Nubian Shield. Geology 18, 1103–1106.

Stevens, R.E., 1944. Composition of some chromites of the Western Hemisphere. American Mineralogist 29, 1–34.

Sturchio, N.C., Sultan, M., Batiza, R., 1983. Geology and origin of Meatiq dome, Egypt: a Precambrian metamorphic core complex? Geology 11, 72–76.

Unzog, W., Kurz, W., 2000. Progressive development of lattice preferred orientations (LPOs) of naturally deformed quartz within a transpressional collision zone (Panafrican Orogen in the Eastern Desert of Egypt). Journal of Structural Geology 22, 1827–1835.

Wallbrecher, E., Fritz, H., Khudeir, A.A., Farahad, F., 1993. Kinematics of Panafrican thrusting and extension in Egypt. In: Thorweihe, U., Schandelmeier, H. (Eds.), Geoscientific Research in Northeast Afrika, pp. 27–30.

Witt, W.K., Vanderhor, F., 1998. Diversity within a unified model for Achaean gold mineralization in the Yilgarn Craton of Western Australia: an overview of the late-orogenic structurally controlled gold deposits. Ore Geology Reviews 13, 29–64.

Zang, W., Fyfe, W.S., 1995. Chloritization of the hydrothermally altered bedrocks at the Igarapé Bahia gold deposit, Carajás, Brazil. Mineral Deposits 30, 30–38.

Zoheir, B.A., 2008a. Structural controls, temperature-pressure conditions and fluid evolution of orogenic gold mineralisation in Egypt: a case study from the Betam gold mine, south Eastern Desert. Mineralium Deposita 43, 79–95.

Zoheir, B.A., 2008b. Characteristics and genesis of shear zone-related gold mineralization in Egypt: a case study from the Um El Tuyor mine, south Eastern Desert. Ore Geology Reviews 34, 445–470.

Zoheir, B.A., Lehmann, B., 2011. Listvenite–lode association at the Barramiya gold mine, Eastern Desert, Egypt. Ore Geology Reviews 39, 101–115.